XIII. PLASMAS AND CONTROLLED NUCLEAR FUSION

A. Active Plasma Systems*

Academic and Research Staff

Prof. A. Bers
Prof. G. D. Bernard
Prof. W. D. Getty
Prof. J. G. Siambis
Prof. J. Taillet

Graduate Students

R. R. Bartsch
S. R. J. Brueck
J. A. Davis
F. N. Herba
B. R. Kusse
M. A. Lieberman
J. A. Mangano
R. R. Parker
D. M. Perozek
R. D. Reilly
H. M. Schneider
R. N. Wallace

1. SYSTEM C: ION-CYCLOTRON WAVE GENERATION

We have continued to study generation and propagation of waves in System C near the ion-cyclotron frequency. Since the last report, we have installed a coil in the center of the system, midway between anode and collector (see Fig. XIII-1). The coil consists of 9 turns of No. 16 wire insulated by ceramic tubing and supported by stainless-steel wires arranged in such a way as to minimize electrostatic coupling. We are now investigating ion-cyclotron wave generation by the coil and comparing its efficiency of wave generation with that by concentric electrodes.[1] In this report we discuss a theory of wave generation by the coil and compare it with preliminary experimental results.

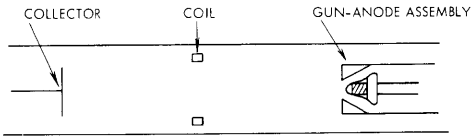

Fig. XIII-1. Illustrating coil position.

Theoretical Discussion

We consider a uniform column of plasma of length L and radius a, surrounded by a perfectly conducting cylinder of radius c, and driven by a circular current filament of radius b. (See Fig. XIII-2). We denote by z the distance from the coil, and assume perfect electric shorts at $z = \pm\frac{L}{2}$. We assume that the dynamics of the plasma can be accounted for by a local dielectric tensor, $\overline{\overline{K}}(\omega)$, of the form

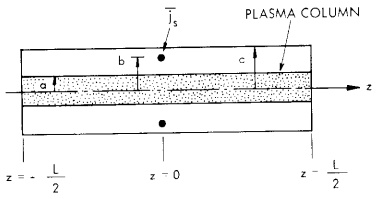

Fig. XIII-2. Illustrating the problem.

---

*This work was supported by the National Science Foundation (Grants GK-57 and GK-614).

$$\overline{\overline{K}} = K_{\perp}\overline{\overline{\delta}} + K_x \hat{i}_z \times \overline{\overline{\delta}} + K_{\parallel}\hat{i}_z\hat{i}_z.$$

The scalars $K_{\perp}$, K_x, and $K_{\parallel}$ have various forms that depend on the model assumed for the plasma. For example, if one assumes cold, collisionless plasma one has

$$\left.\begin{aligned} K_{\perp 0} &= \frac{\omega_{pi}^2}{\omega_{ci}^2 - \omega^2} + \frac{\omega_{pe}^2}{\omega_{ce}^2 - \omega^2} + 1 \\ K_{x0} &= j\frac{\omega\omega_{pi}^2/\omega_{ci}}{\omega_{ci}^2 - \omega^2} + j\frac{\omega\omega_{pe}^2/\omega_{ce}}{\omega_{ce}^2 - \omega^2} \\ K_{\parallel 0} &= -\frac{\omega_{pi}^2}{\omega^2} - \frac{\omega_{pe}^2}{\omega^2} + 1, \end{aligned}\right\} \tag{1}$$

while, for a plasma with ion-electron collisions one has

$$\overline{\overline{K}}_{\eta} = \left(\overline{\overline{K}}_0^{-1} + j\omega\epsilon_0\eta\overline{\overline{\delta}}\right)^{-1}, \tag{2}$$

where η is the resistivity (assumed to be a scalar). Ion-neutral collisions may be accounted for in a phenomenological way by replacing the ion mass in set (1) by $m_i(1 + \upsilon/j\omega)$, where υ is the ion-neutral collision frequency for momentum transfer. The problem is now simply formulated by Maxwell's equations

$$\nabla \times \overline{H} = j\omega\epsilon_0\overline{\overline{K}} \cdot \overline{E} + \overline{j}_s \tag{3}$$

$$\nabla \times \overline{E} = -j\omega\mu_0\overline{H}, \tag{4}$$

where $\overline{j}_s = NI\delta(r-b)\,\delta(z)\,\hat{i}_{\theta}$ accounts for the current in the coil. The boundary condition is zero tangential electric field. The boundary conditions at $z = \pm\frac{L}{2}$ may be eliminated by replacing the geometry of Fig. XIII-2 with a cylinder of infinite extent driven by the current source

$$\overline{j}_s' = \sum_{n=-\infty}^{\infty} (-1)^n \overline{j}_s(z-nL).$$

If, then, Eq. 3 (with $\overline{j}_s$ replaced by $\overline{j}_s'$) and Eq. 4 are Fourier-analyzed in the z-direction, we obtain the following equation for the transverse component of the electric field, $\overline{E}_T$,

$$\nabla_T \times \nabla_T \times \bar{\bar{E}}_T - \nabla_T \frac{1}{K_{||}} \nabla_T \cdot \bar{\bar{K}}_T \cdot \bar{E}_T - k_0^2 \bar{\bar{K}}_T \cdot \bar{E}_T + \beta^2 \bar{\bar{E}}_T =$$

$$-\hat{i}_\theta j\omega\mu_0 NI \times \delta(r-b) \times \sum_{n=-\infty}^{\infty} (-1)^n e^{-jn\beta L}. \qquad (5)$$

Here, ∇_T is the transverse part of ∇, $\bar{\bar{K}}_T$ is the transverse part of $\bar{\bar{K}}$, and $k_0 = \omega/c$.

A formal solution to Eq. 5 may be obtained by expanding $\bar{E}_T$ and the right-hand side of Eq. 5 in terms of the eigenvectors of the equation

$$\nabla_T \times \nabla_T \times \bar{e} - \nabla_T \frac{1}{K_{||}} \nabla_T \cdot \bar{\bar{K}}_T \cdot \bar{e} - k_0^2 \bar{\bar{K}}_T \cdot \bar{e} + k^2 \bar{e} = 0. \qquad (6)$$

To do this we need the eigenvectors of the adjoint equation

$$\nabla_T \times \nabla_T \times \bar{\epsilon} - \bar{\bar{K}}_T^\dagger \cdot \nabla_T \frac{1}{K^*} \nabla_T \cdot \bar{\epsilon} - k_0^2 \bar{\bar{K}}_T^\dagger \cdot \bar{\epsilon} + \ell^2 \bar{\epsilon} = 0, \qquad (7)$$

where the symbol $(\,)^\dagger$ denotes complex-conjugate transpose. The boundary conditions for Eq. 6 are tangential $\bar{e}$ and $\nabla_T \cdot \bar{\bar{K}}_T \cdot \bar{e}$ equal to zero on the boundary, while boundary conditions for Eq. 7 are tangential $\bar{\epsilon}$ and $\nabla_T \cdot \bar{\epsilon}$ equal to zero on the boundary. In terms of the assumed complete set $\bar{e}_i$ of solutions to Eq. 6 and the set $\bar{\epsilon}_j$ of solutions to Eq. 7, we may obtain a formal solution to Eq. 5 which, after performing the inverse Fourier transform in the z-direction, becomes

$$\bar{E}_T = -j\omega\mu_0 NI \sum_i \frac{b\bar{\epsilon}_i^* \cdot \hat{i}_\theta \big|_{r=b} \bar{e}_i}{\int_0^c r\, dr\, \bar{\epsilon}_i^* \cdot \bar{e}_i} \cdot \frac{1}{2k_i} \cdot \frac{\sin k_i\left(\frac{L}{2} - |z|\right)}{\cos \frac{k_i L}{2}}, \qquad (8)$$

where the k_i are the eigenvalues of Eq. 6. The problem is then completely solved by obtaining the eigenvalues and eigenvectors of (6).

An assumption often made in treating problems of this sort[2] is that of zero electron mass, which, from the point of view of Eq. 6 removes the term $\nabla_T \frac{1}{K_{||}} \nabla_T \cdot \bar{\bar{K}}_T \cdot \bar{e}$. The resulting solution involves a discontinuity in $\bar{\bar{K}}_T \cdot \bar{e}$, a feature that is inconsistent with the assumption that $\nabla_T \frac{1}{K_{||}} \nabla_T \cdot \bar{\bar{K}}_T \cdot \bar{e}$ is small in comparison with other terms. We are working on other approximate solutions to (6) which have more validity for the conditions of our experiment.

One feature of Eq. 8, which is apparent even without detailed knowledge of $\bar{\epsilon}_i$ and $\bar{e}_i$, is the possibility of a body resonance slightly below ω_{ci}, where $k_i L \sim \pi$. This suggests the possibility of efficient coupling of energy to the ions by exciting this resonance.

Experimental Results

The frequency dependence of $B_z = \frac{1}{j\omega} \nabla_T \times \bar{E}_T$ near ω_{ci} has been measured by using

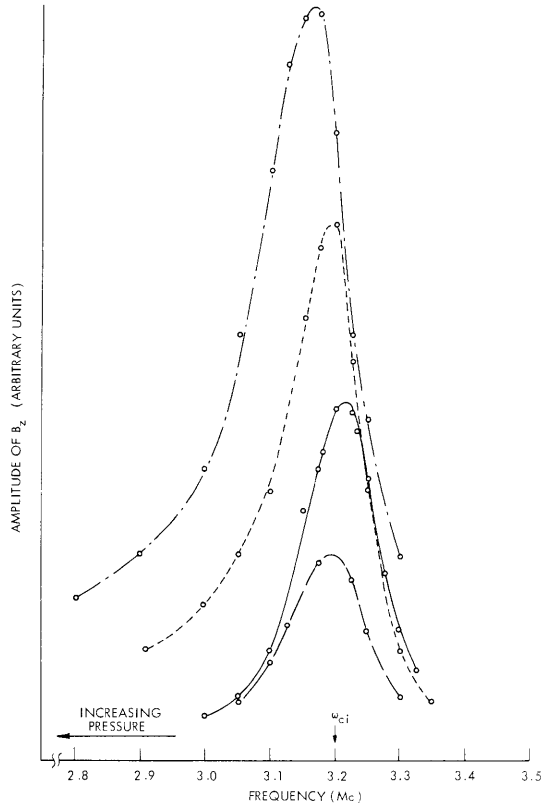

Fig. XIII-3.
Amplitude of B_z versus frequency for four pressures 100 μsec after turn-off. The pressures are in the ratio 1:1.3:1.7:3.4.

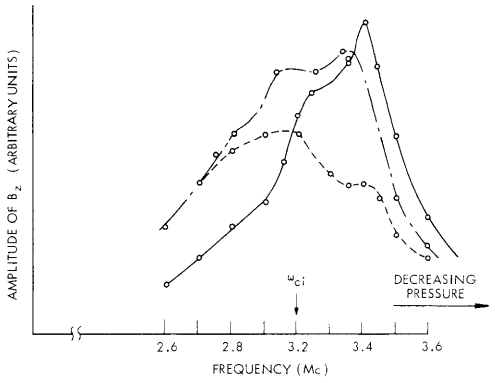

Fig. XIII-4. Amplitude of B_z versus frequency for three pressures at turnoff. The pressures are in the ratio 1:2:3.

a small pickup coil positioned approximately midway between the anode and the driving coil against the wall. Two sets of results are shown in Fig. XIII-3 and XIII-4. The curves of Fig. XIII-3 were obtained with a low-power beam (3 kV and 7 amps) 100 μsec after turnoff, and appear to be associated with a resonance of the usual type. The curves of Fig. XIII-4 were obtained with a higher power beam and were taken immediately after turnoff. We believe that the resonance that develops below ω_{ci} for

increasing pressure (and therefore density) may be associated with the body resonance discussed above.

R. R. Parker

References

1. R. R. Parker, Quarterly Progress Report No. 81, Research Laboratory of Electronics, M.I.T., April 15, 1966, pp. 72-75.
2. T. H. Stix, The Theory of Plasma Waves, (McGraw-Hill Book Company, New York, 1962.

2. BEAM-PLASMA DISCHARGE: SYSTEM D

Introduction

During the last quarter studies were made of the plasma density and electron temperature in System D. The results of different methods of density measurements agree reasonably well, although further refinements must be made. The direct measurements of density made thus far are by the methods of fundamental cavity-mode shift, higher order cavity-mode shift, 8-mm Fabry-Perot interferometry, and 4-mm interferometry. The density range covered by these four approached is 10^9-10^{14} cm^{-3}. There are regions of overlap between methods so that a check for consistency is possible.

The density measurements require additional data concerning the density profile. These data are not yet available and consequently there is some spread in the results of the four methods. In the fundamental mode-shift measurement, uncertainty about the exact cavity mode that was used may account for differences between this and the other measurements.

The 4-mm interferometer is used to measure the density during the electron beam pulse (see Sec. XIII-A. 3). Under the assumption that the plasma is 10 cm in diameter, a typical average density of 5×10^{12} cm^{-3} is found during the beam pulse. A sharp drop in density occurs in the first few milliseconds after beam turnoff, and the plasma enters a decay period in which the loss rate is determined by electron-neutral scattering. During the decay period the density is tracked by the 8-mm interferometer and the mode-shift technique. These methods, at present, agree within a factor of 5 but it is expected that further refinements will lead to better agreement. The density is typically 10^{11} cm^{-3} at 20 msec after beam turnoff for a hydrogen pressure in the range of 10^{-4} Torr. The plasma consists of a cold-electron component and approximately a 1% hot-electron component during this decay period.

Electron temperature measurements were made by spectrographic methods. The measurements are discussed in detail in Section XIII-A. 4. The result of this measurement is that the electrons have an effective temperature of 4-5 electron volts. This is

presumably indicative of the average energy of the cold electrons in the plasma. The measurement was made during the electron beam pulse. The hot-electron component has an average energy of the order of 10 keV, and is evidenced by the generation of x radiation, diamagnetism, and the long decay time of the plasma.

The cold-electron temperature in System C has been measured by the same spectrographic technique (see Sec. XIII-A. 4), and checked by Langmuir probe measurements. The results are in qualitative agreement, and temperatures of 5 to 10 eV are obtained. In both Systems C and D, we find consistency between the temperature, density, and diamagnetism. The diamagnetic signals are almost entirely caused by the hot-electron component.

Gas Injection System

The peak pressure during the gas pulse has been determined for the Asco-valve injection apparatus now in use. A steady gas feed was found to give the same plasma diamagnetism during the beam pulse when the pressure in the system was adjusted to $2\text{-}3 \times 10^{-5}$ mm Hg as measured by a Veeco gauge. The true hydrogen pressure is approximately seven times higher than the measured value.[1] The boundary between a weak discharge and an intense discharge as determined by the diamagnetism during the

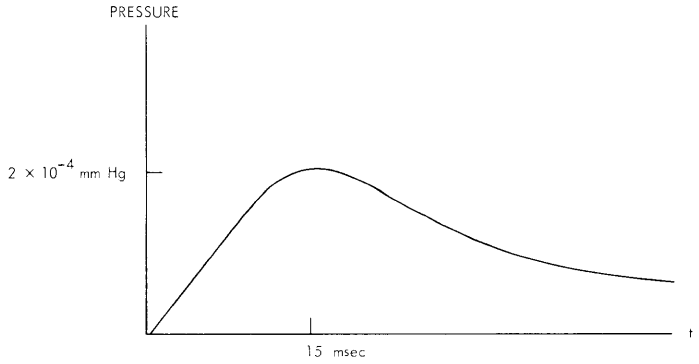

Fig. XIII-5. Asco valve pressure transient for adjustment that gives the longest plasma density decay.

beam pulse was found to be well defined when the steady-flow gas pressure was varied. Figure XIII-5 shows the pressure transient for the Asco-valve system.

Construction has been completed on the Marshall (shock-wave) valve[2] shown in Fig. XIII-6. Preliminary tests with a nude 6AH6 pressure transient sensor indicate that the Marshall valve is faster than the Asco valve. The pressure transient is shown in Fig. XIII-7. Additional speed will be obtained by removing the beam stop shown in Fig. XIII-8. An electric drive is now under construction.

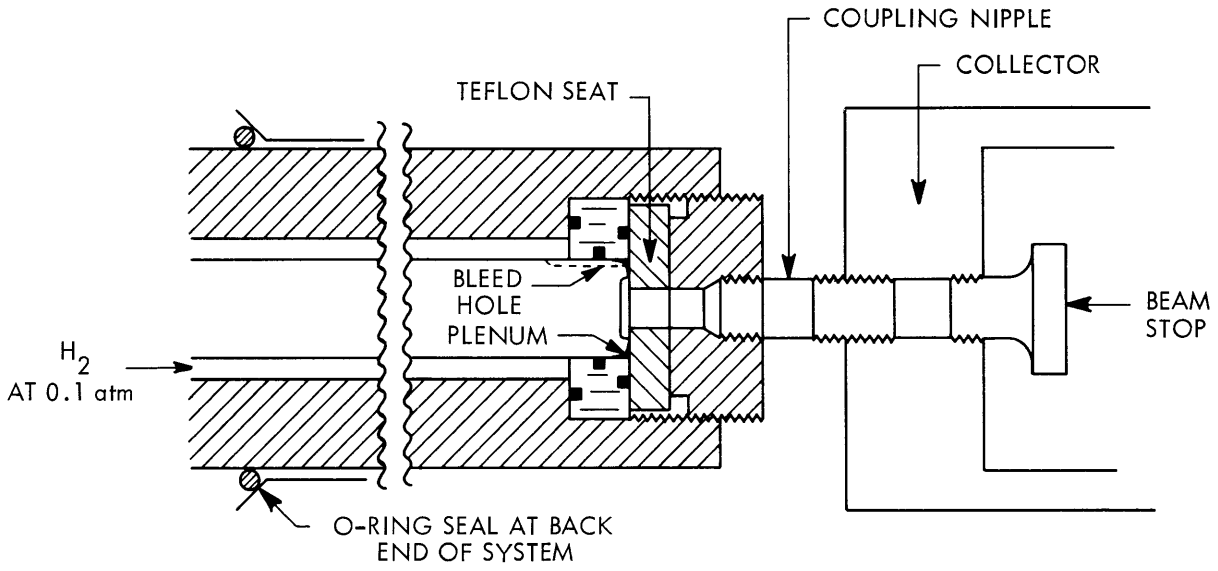

Fig. XIII-6. Marshall valve.

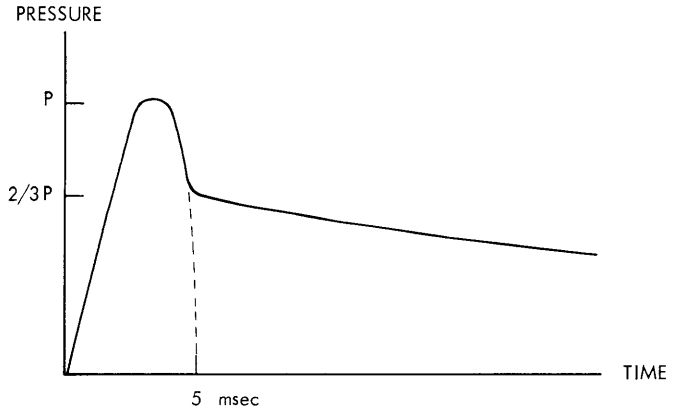

Fig. XIII-7. Marshall valve pressure transient.

Light and Plasma Diamagnetism Measurements

The light transient for a typical discharge is shown in Fig. XIII-8. The peak pressure of the gas pulse for the case shown is 15-50% above the minimum necessary for an intense discharge. The delay between the start of the gas injection and the firing of the electron beam was adjusted so that the beam fired just before the peak of the pressure pulse. The pressure transient is also shown in Fig. XIII-8. The final decay rate of the light signal is observed to be ~20 msec, which is the final decay rate observed for the electron density for the pressure transient shown. Since the light output is roughly proportional to the product of electron density and pressure, the light transient can be used to extrapolate the electron density[1] back to the end of the beam pulse. The resulting density is $\sim 10^{12}$ cm^{-3}, if the pressure is assumed to be constant.

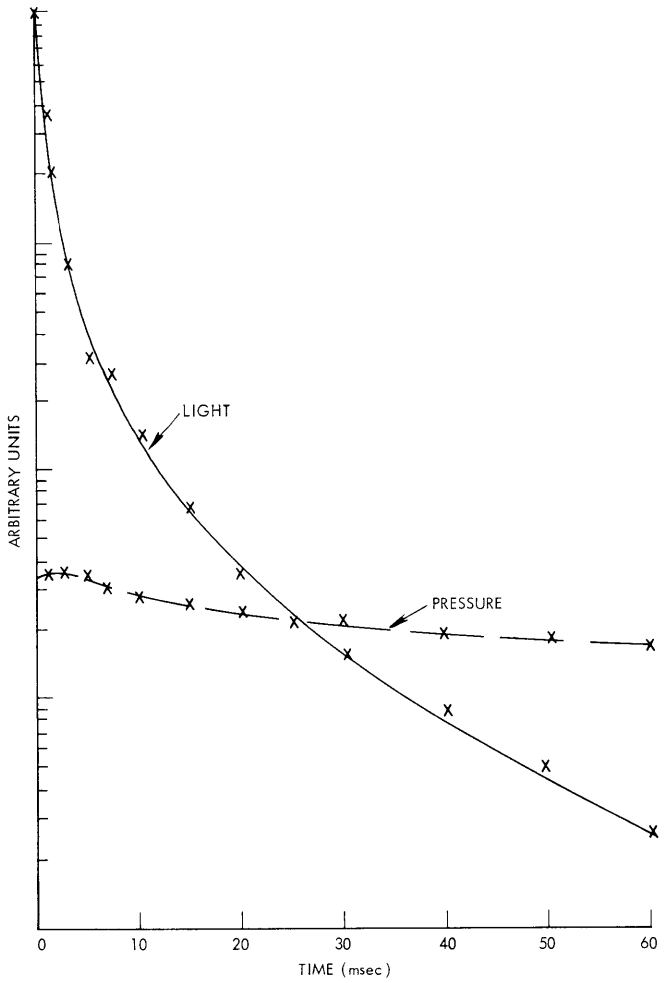

Fig. XIII-8. Light and pressure transient.

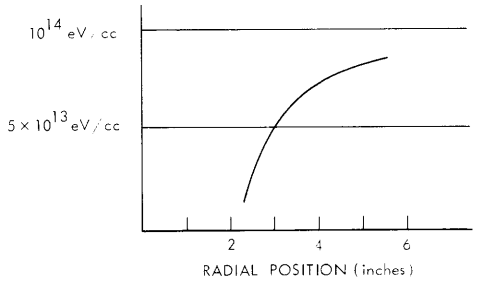

Fig. XIII-9. Perturbation of plasma diamagnetism by a Langmuir probe.

The initial decay time constant of the plasma diamagnetism due to the hot electrons is listed in Table XIII-1.

Table XIII-1. Initial diamagnetic decay time constant as a function of peak pressure.

Peak Pressure	$\tau_{k/e}$
3×10^{-4}	15.6 msec
6×10^{-4}	10.2
2×10^{-3}	4.7
9×10^{-3}	1.55

Langmuir probes used to measure the plasma profile were found to alter the discharge. The amplitude of the plasma diamagnetism as a function of the radial position of a tungsten ball of 0.040 inch diameter is shown in Fig. XIII-9.

Plasma Density Measurements

(i) 8-mm Interferometer Density Measurement

Plasma density measurements have been made up to approximately 10^{12} cm^{-3} with the Fabry-Perot interferometer arrangement shown in Fig. XIII-10. The shift of the

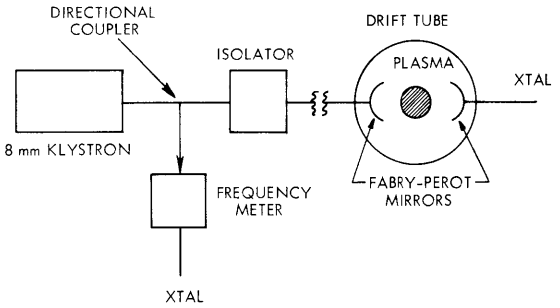

Fig. XIII-10. Fabry-Perot interferometer.

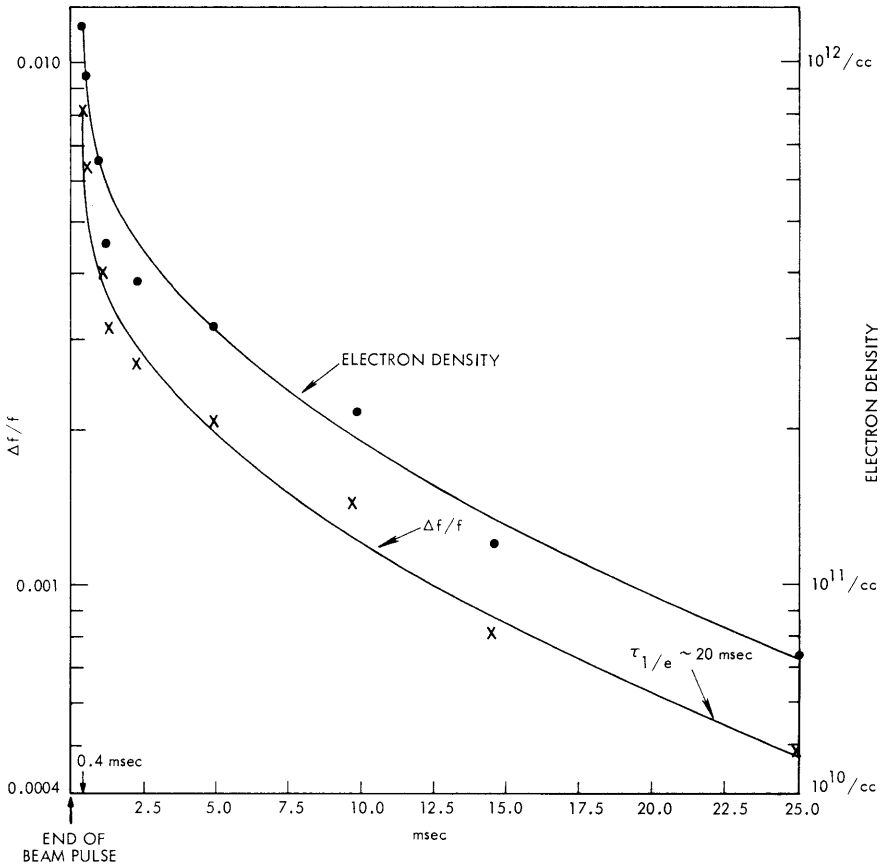

Fig. XIII-11. Fabry-Perot electron density measurement.

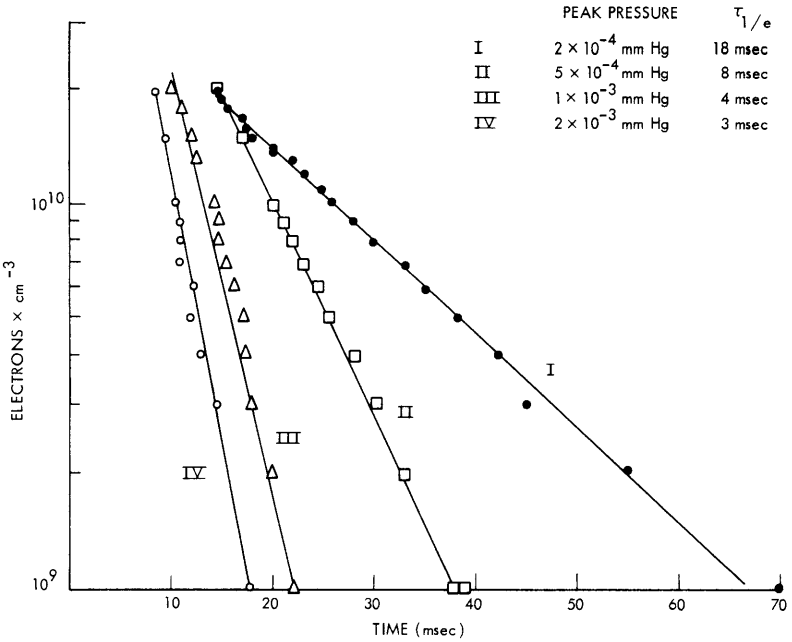

Fig. XIII-12. Density decay as a function of peak pressure.

resonant frequency of the cavity formed by the spherical horns is related to the plasma density by

$$\frac{\Delta f}{f} = \frac{1}{4R} \frac{2 \int_0^{R_p} n_e(r)\, dr}{(2\pi f)^2} \frac{e^2}{m_e \epsilon_o},$$

where R is the drift-tube radius R_p is the plasma radius, f is the resonant frequency of the Fabry-Perot cavity (31.225 kMc), $n_e(r)$ is the electron density profile, e is the electronic charge, m_e is the electronic mass, the ϵ_o is the dielectric constant of free space. $\Delta f/f$ is shown in Fig. XIII-11 for a discharge adjusted for long decay ($\tau_{1/e} \sim 20$-30 msec). The plasma density shown in Fig. XIII-11 is found from the mode-shift information by assuming that the plasma density is given by

$$n_e(r) = \begin{cases} n_e(0)\, J_o\left(\frac{2.405\, r}{R_p}\right) & 0 \leq r \leq R_p \\ 0 & R \geq r \geq R_p \end{cases}$$

$$R_p = \frac{1}{3} R.$$

(ii) UHF density measurement

UHF mode-shift density measurements have been made in which the cavity was excited with E probes in the end of the system. The density has been tracked back into the discharge to 2×10^{10} cm^{-3}. The density decay as a function of pressure is determined from the pressure measurement discussed above, and is not the same as that assumed previously.[3] The results of the measurement are shown in Fig. XIII-12, where the density decay is plotted for several pressures.

The authors wish to acknowledge the use of the facilities of the National Magnet Laboratory for this experiment.

R. R. Bartsch, W. D. Getty

References

1. T. J. Fessenden and M. A. Lieberman, private communication.
2. J. Marshall in Plasma Acceleration, edited by S. W. Kash (Stanford University Press, California, 1960), pp. 61-62.
3. R. R. Bartsch, Quarterly Progress Report No. 81, Research Laboratory of Electronics, M.I.T., April 15, 1966, p. 69.

3. ELECTRON DENSITY MEASUREMENTS FOR BEAM PLASMA SYSTEMS WITH A 4-mm INTERFEROMETER

To obtain accurate electron density information with a minimum of discharge perturbation, a 4-mm microwave interferometer was used on Beam-Plasma Discharge Systems C and D. Such an interferometer measures the propagation constant of the plasma medium which may, under certain conditions, be simply related to the time-variant electron density.

The interferometer circuit (shown in Fig. XIII-13) consists of two microwave signal paths – a plasma path and a reference path. The sum and difference signals from the balanced mixer are each square-law-detected by crystals. The difference between the two detected signals is a measure of the amplitude and phase of the signal transmitted through the plasma. If the interferometer signal frequency is much higher than the plasma frequency, the plasma appears transparent, and there is essentially no amplitude change caused by attenuation in the plasma path. In the absence of a plasma the variable phase shifter in the reference path is adjusted to null the output signal. The output signal during the transient discharge is then proportional to the sine of the phase difference between the two paths and is therefore a measure of the phase constant of the plasma as a function of time.

Since the microwave horns and lenses focus the microwave radiation into a beam whose diameter is approximately 1/3 of the plasma diameter, the cylindrical plasma may be considered as a slab and the problem is reduced to one dimension.[1] The phase constants of the vacuum and plasma are

$$\beta_v = \frac{2\pi}{\lambda} \tag{1}$$

$$\beta_p = \left[1 - \left(\frac{\omega_p}{\omega}\right)^2\right]^{1/2} \qquad \beta_v = \left[1 - \frac{n}{n_c}\right]^{1/2} \beta_v \tag{2}$$

when the microwave electric field is parallel to the static magnetic field, and collision frequency $\nu \ll \omega$. The critical density n_c is given by

$$n_c = m\epsilon_o\omega^2/e^2.$$

The phase shift that is due to the presence of the plasma is therefore

$$\Delta\phi = -\int [\beta_p - \beta_v]\, dx \tag{3}$$

or, in terms of Eqs. 1 and 2,

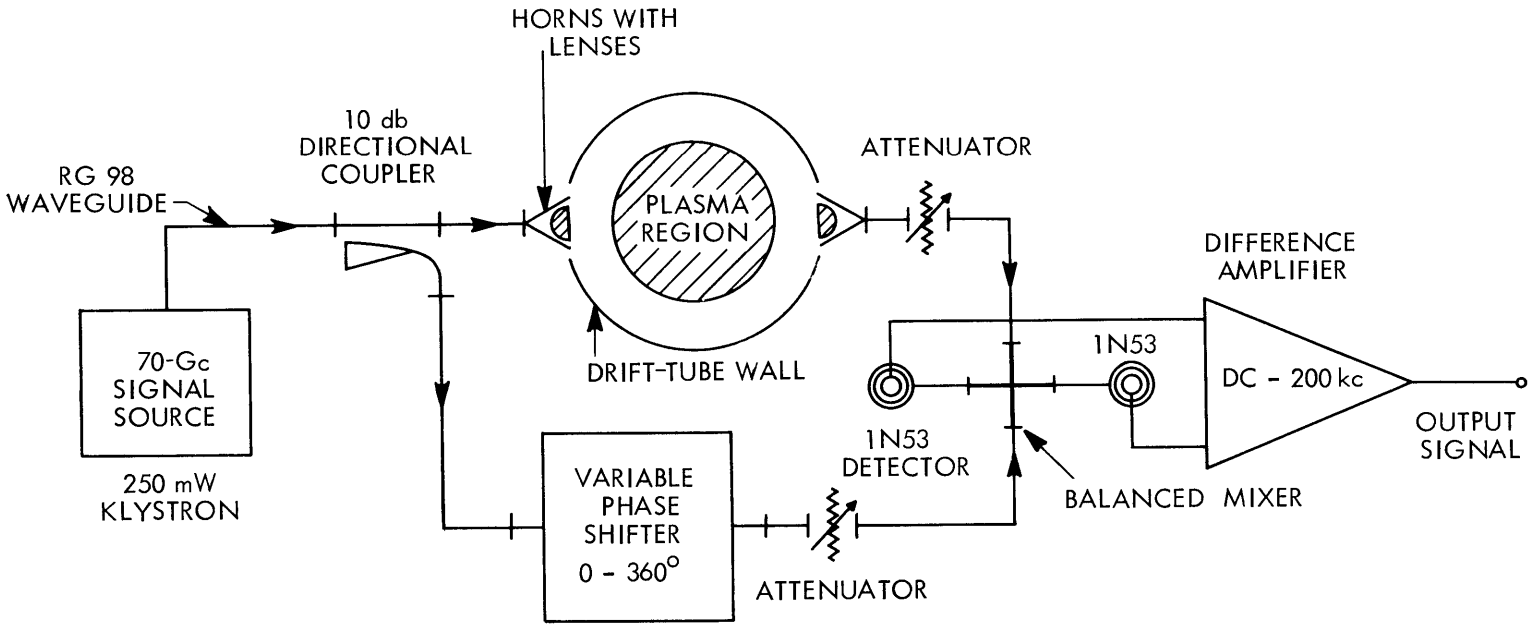

Fig. XIII-13. Four-millimeter interferometer system.

$$\Delta\phi = \int \left\{ 1 - \left[1 - \frac{n(x)}{n_c} \right]^{1/2} \right\} \frac{2\pi}{\lambda}\, dx \tag{4}$$

which to first order in $n(x)/n_c$ is

$$\Delta\phi = \frac{\pi}{\lambda n_c} \int n(x)\, dx. \tag{5}$$

Hence, the relation between density and phase shift is

$$\int n(x)\, dx = \frac{\lambda n_c}{\pi}\, \Delta\phi = \frac{2\epsilon_o mc\omega\, \Delta\phi}{e^2}. \tag{6}$$

Since only the integral of the spatially varying electron density is given explicitly, independent knowledge of the density profile is required for quantitative measurements. A spatially averaged electron density may be obtained, however, by assuming a rectangular profile. For such a rectangular profile the integration of Eq. 6 is trivial, and gives

$$n_{av} = \frac{2\epsilon_o mc\omega\, \Delta\phi}{e^2 L} \quad \text{for } n \ll n_c. \tag{7}$$

In practical units, this equation can be written

$$n_{av} = \frac{2.6 \times 10^{13}}{L} \frac{\Delta\phi}{\pi}\ (\text{cm}^{-3}),$$

where $\Delta\phi$ is in radians, and L in centimeters. The parameter L is the effective width of the profile and is estimated experimentally by using a Langmuir probe.

Results

Density measurements were made on Beam-Plasma Discharge Systems C and D against system parameters such as axial magnetic field, beam voltage, and pressure. Representative results of these measurements are given in Figs. XIII-14 through XIII-17.

Figure XIII-14 shows the variation with electron beam voltage and axial magnetic field of the value of n_{av} during the beam pulse. It was observed that the integral of the density over the profile, Eq. 6, is nearly independent of the magnetic field; however, Langmuir probe data indicate that the effective width of the profile decreases with increasing field, giving rise to the spread in n_{av} between these curves.

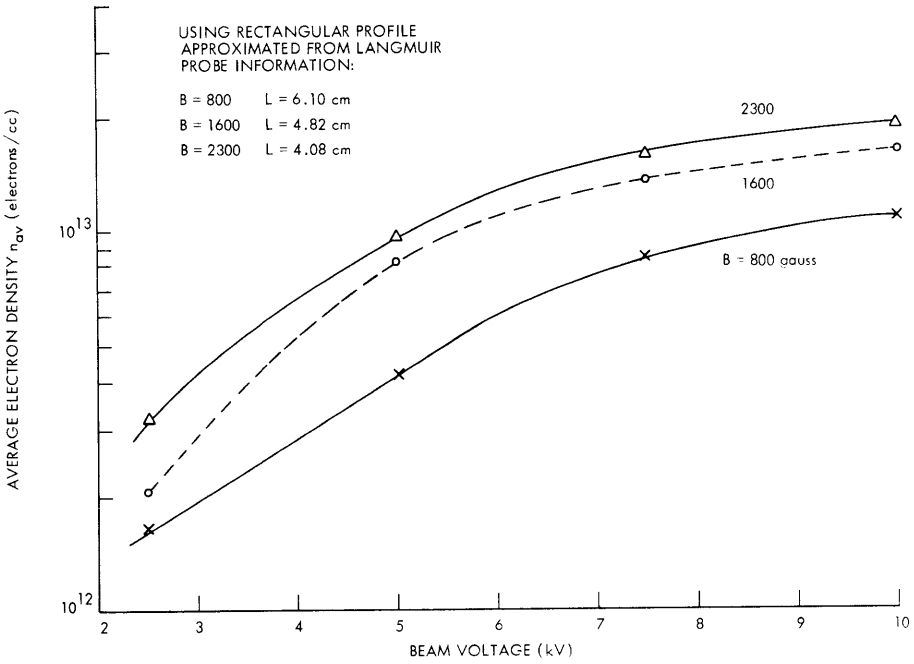

Fig. XIII-14. Average electron density in System C as a function of electron beam voltage for three values of midplane magnetic flux density. Hydrogen pressure for these curves was approximately 2×10^{-4} Torr.

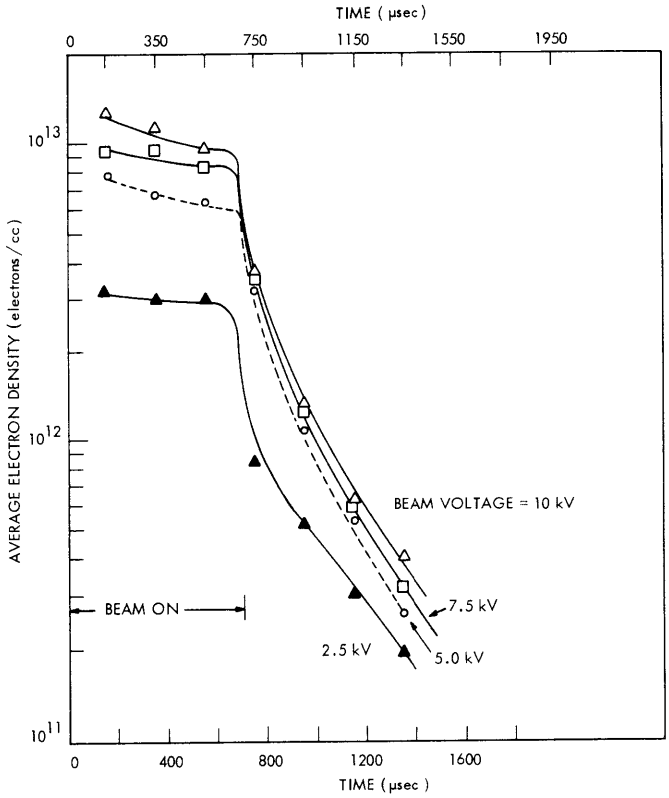

Fig. XIII-15.
Density decay in System C for various electron-beam voltages. Hydrogen pressure, 2×10^{-4} Torr; midplane magnetic flux density, 2300 gauss; assumed plasma width, L = 4.08 cm.

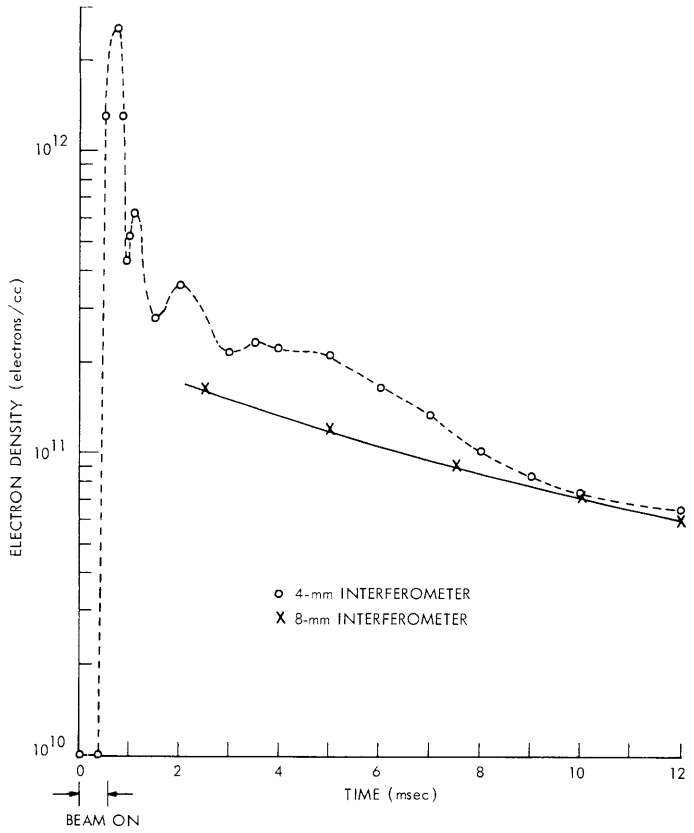

Fig. XIII-16. Density decay in System D. Assumed plasma width, L = 10 cm. 8-mm Fabry-Perot interferometer data from Section XIII-A. 2 are shown.

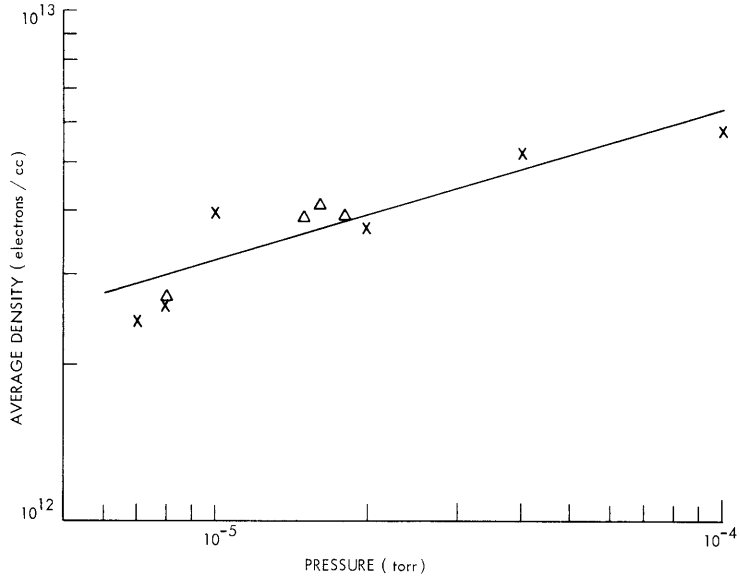

Fig. XIII-17. Variation of average density during beam pulse as a function of gas pressure for System D. Assumed plasma width, L = 10 cm.

The density during the beam pulse is nearly constant at low operating pressures, but at higher pressures it may fluctuate considerably. The frequency of the fluctuations may be measured from the interferometer output signal and is of the order of 10-50 kc. The density decays smoothly in the afterglow period that begins at beam turn-off.

The density decay of the plasma was also measured. The sensitivity of the interferometer was sufficiently high to allow the density to be measured for 2 msec in the afterglow of System C and 20 msec in System D. Figures XIII-15 and XIII-16 show the density decay in Systems C and D, respectively. The observed decay rates for both Systems C and D are in agreement with their expected values. For System C, the plasma loss rate is determined by the rate of ion effusion out of the system. This rate is approximately $2\overline{v}_i/\ell$, where $\overline{v}_i$ is the average ion velocity, and ℓ is the length of the system. The plasma loss rate is determined by the ions in this case because no magmetic mirrors were used to reduce plasma end loss, and the plasma potential was therefore positive. The value of $2\overline{v}_i/\ell$ for room temperature ions is 250-300 μsec; the curves in Fig. XIII-15 exhibit decay times of 350-400 μsec. The plasma in System D contains a hot-electron component with an average energy of the order of 10 keV, and is confined by magnetic mirrors. The loss rate is determined by the rate of scattering of the hot electrons into the mirror loss cones.[2] The decay curve of Fig. XIII-16 is typical for System D and indicates that the decay time is approximately 5 msec. This is in qualitative agreement with other measurements and with calculated values of decay time.[3] The results of microwave measurements (see Sec. XIII-A. 2) with a Fabry-Perot interferometer at 8 mm are shown in Fig. XIII-16 for comparison with the 4-mm results. A plasma width of 10 cm was assumed for both cases.

The variation as a function of pressure of the average density during the beam pulse is shown in Fig. XIII-17 for System D. This graph shows the general tendency of the plasma density to increase with pressure. Relative values of pressure are used in Fig. XIII-17.

D. M. Perozek, W. D. Getty

References

1. M. A. Heald and C. B. Wharton, Plasma Diagnostics with Microwaves (John Wiley and Sons, Inc., New York, 1965), pp. 120-121.

2. T. J. Fessenden, Sc. D. Thesis, Department of Electrical Engineering, M. I. T., 1965, p. 96.

3. R. R. Bartsch, Quarterly Progress Report No. 81, Research Laboratory of Electronics, M. I. T., April 15, 1966.

4. SPECTROGRAPHIC MEASUREMENT OF ELECTRON TEMPERATURE IN THE BEAM-PLASMA DISCHARGE

The visible radiation emitted from a hydrogen plasma contains information about the average kinetic energy of the electrons. Emitted radiation is of two types; spectral lines (the Balmer series) and a continuum produced by recombination and Bremsstrahlung. The emitted intensities of line and continuum radiation are functions of temperature and, furthermore, the temperature dependences of the two are different. Griem[1] gives quantum-mechanical calculations that result in the temperature dependence of the ratio of the total line intensity and the total continuum intensity in a 100 Å band about the line. This result was used to find the electron temperatures of two plasmas from spectroscopic data. The two quantities whose ratio determines the temperature are shown in Fig. XIII-18.

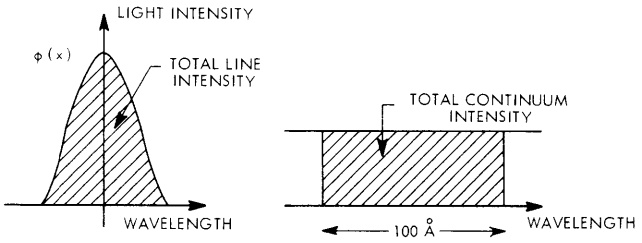

Fig. XIII-18. Areas of the line intensity and continuum intensity used for calculating the electron temperature.

The wavelength broadening of a Balmer line observed in the laboratory is due largely to distortions caused by the spectrometer. To obtain the true spectral line shape $\phi(x)$ from the measured spectrum, $f(x)$, the following integral equation must be solved:

$$f(x') = \int_{-\infty}^{\infty} a(x'-x)\, \phi(x)\, dx,$$

where $a(x)$ is an "apparatus function." The apparatus function is the apparent broadened spectral profile given to monochromatic light, whose true spectrum is a line of zero width, and it is measured experimentally for each entrance slit width to be used. The apparatus function was also calculated theoretically. In this work the integral equation was solved for $\phi(x)$ by use of Voigt functions, which are tabulated functions that can be fitted to experimental $a(x)$ and $f(x)$ and used to solve easily for $\phi(x)$. The details of the calculations are given elsewhere.[2]

For data taking, the entrance slit of the spectrometer is pointed at a window in the plasma, and a lens is used to collimate the light. A photomultiplier tube collects the

light leaving the exit slit, and its anode current goes through an RC integrator to an oscilloscope. The tube response is in the form of bursts of electrons which can be seen individually if the light intensity falling on the tube is low. Each burst corresponds to an individual primary photoelectron. The integrating circuit counts the number of pulses occurring during the integration time, which is taken to be the beam pulse length.

Table XIII-2. System D.

	Peak pressure = 2×10^{-4} Torr		
Midplane Magnetic field (gauss)	550	1000	1200
Electron temperature (ev)	4.3	4.0	3.5
	Peak pressure = 10^{-5} Torr		
Electron temperature (ev)	-	4.0	-

Table XIII-3. System C.

	Peak pressure = 6×10^{-5} Torr		
Beam voltage (kv)	6.5	8	9
Beam current (amps)	15	22	30
Electron temperature (ev)	4	4	5

The measured spectrum f(x) is the variation with wavelength of the output voltage of the integrating circuit as the spectrometer is scanned across the line. A 15-μ entrance slit was used for line measurements and a 1000-μ slit was used for the continuum, the wide slit being necessary because the intensity was weak. The integral equation was solved for $\phi(x)$ and the height of the continuum, with the use of experimental apparatus functions for 15- and 1000-μ slits. The areas under the line and a 100 Å band of continuum were computed, and their ratio was used to find the electron temperature.

Data were taken on Beam-Plasma Discharge Systems C and D under various operating conditions. The results are shown in Tables XIII-2 and XIII-3.

R. D. Reilly, W. D. Getty

References

1. H. R. Griem, Plasma Spectroscopy (McGraw-Hill Publishing Company, New York, 1964).
2. R. D. Reilly, S.M. Thesis, Department of Electrical Engineering, M.I.T., June 1966.

5. COMPUTER SIMULATION OF THE BEAM-PLASMA DISCHARGE

This quarter we continued[1] modelling the beam-plasma discharge by means of one-dimensional charge sheets. This time, however, we required the plasma to remain linear, and represented only the beam with sheets. The plasma is represented by its equivalent dielectric constant

$$\epsilon(\omega_1 k) = \epsilon_o\left[1 - \frac{\omega_p^2}{\omega(\omega - i\nu)}\right]. \tag{1}$$

In the appendix it is shown that the response of the plasma to a sheet of charge q passing through it is

$$E(z,t) = -\frac{q}{\epsilon_o}\left(1 + \frac{\nu^2}{4\omega_o^2}\right)^{1/2} e^{-\frac{\nu}{2}[t-t_1(z)]} \cos\left\{\omega_o[t-t_1(z)] - \tan^{-1}\frac{\nu}{2\omega_o}\right\} \times \mu_{-1}[t-t_1(z)], \tag{2}$$

where

$$\omega_o^2 = \omega_p^2\left(1-\nu^2/4\omega_p^2\right), \tag{3}$$

and $t_1(z)$ is the time when the sheet passes the point z (if the velocity of the sheet does not reverse). This response is shown in Fig. XIII-19. Since the plasma is assumed to

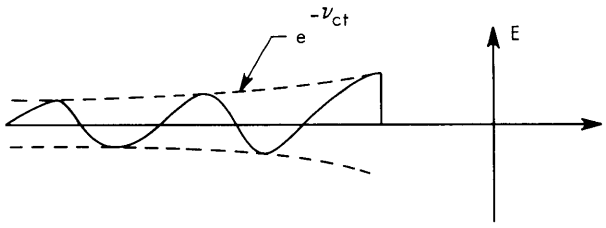

Fig. XIII-19. The electric field produced by a single sheet moving through the plasma. (Actual decay is exaggerated.)

be linear, we can superimpose the responses of the sheets to obtain the response for a continuously injected beam.

The sheets were injected into a previously empty plasma (free of sheets) with a velocity modulation of 2 percent and no density modulation. A Milne numerical integration routine was used to calculate the sheet trajectories. It is

$$x(t+\Delta t) = x(t) + x(t-2\Delta t) - x(t-3\Delta t) + \frac{(\Delta t)^2}{4}[5a(t)+2a(t-\Delta t)-5a(t-2\Delta t)] + \frac{17(\Delta t)^6}{240}\frac{d^6x}{dt^6}.$$

At all points spaced $\Delta x = v_o \Delta t$ apart (in these calculations $\Delta t = 0.2\ \omega_p^{-1}$ the magnitude and phase of the electric field were derived. It is sufficient to specify the magnitude and phase of the electric field at each cell point, since the field attributable to each sheet varies consinusoidally in time, and when cosines add they produce another cosine. Interpolation of the field at a sheet located between two cell points was done by fitting a second-order polynomial to the values at three cell points bracketing the considered sheet. The Runge-Kutta integration method, which requires only present values of x(t), was used to start the Milne formula, which requires x(t) and its value at three previous time steps. The first four time steps were calculated by the Runge-Kutta method.

When sheet crossings occur, there is a discontinuity in the force, and the Milne integration formula, which is derived for a continuous force acting between t and t + Δt, would produce errors if no corrections were made. On crossing, the force attributable to one sheet, q^2/ϵ_o, is added to a(t), a(t-Δt), a(t-2Δt) if the sheet crosses, and subtracted if it does not. This allows the acceleration to be a continuous function of time. This process is justified if it yields the correct acceleration, velocity, and position for times greater than the crossing time. For this to be true, x(t), x(t-Δt), x(t-2Δt), and x(t-3Δt) must also be modified. In Fig. XIII-20 we show how the corrections are made for the crossed sheet. The solid lines represent the old functions, which are correct for times less than the crossing time. The corrected functions, which are correct for times greater than the crossing time, are shown as dashed lines. We assume that the crossing sheet presents a constant force to the crossed sheet over time $(\Delta t)_2$. This is

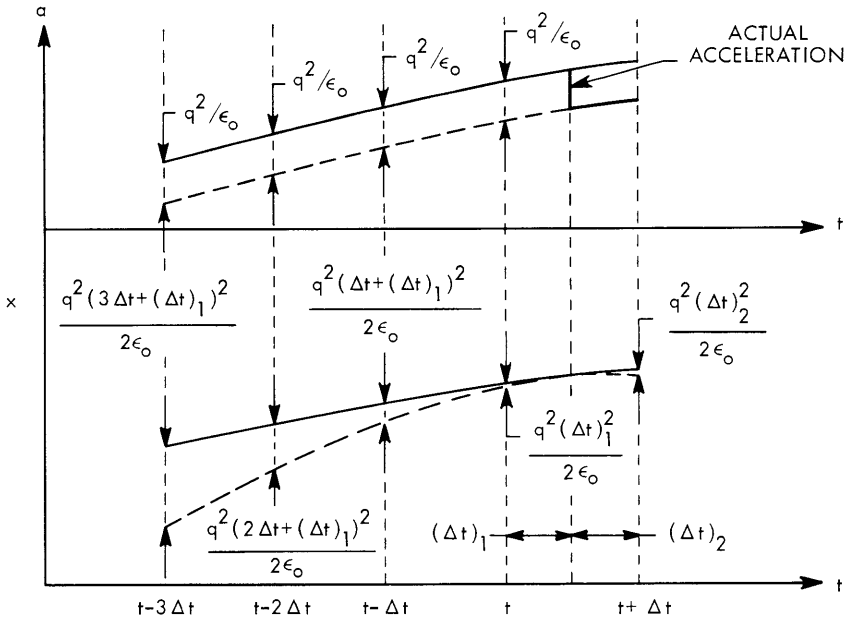

Fig. XIII-20. Corrections made to the acceleration and position to allow for crossings. (Corrections for the crossed sheet are shown.) t + $(\Delta t)_1$ is the time of crossing.

a very good approximation if the sheets have nearly the same velocity. Note that if we reduce the acceleration for $t < t + (\Delta t)_1$, we must increase the previous velocities for the sheet to have the same velocity at the crossing time. This is reflected in the reduced x's for $t < t + (\Delta t)_1$. The time of crossing is estimated by the formula

$$t + (\Delta t)_1 = t + \frac{x_{crossed}(t) - x_{crossing}(t)}{\frac{x_{crossing}(t+\Delta t) - x_{crossing}(t)}{\Delta t} - \frac{x_{crossed}(t+\Delta t) - x_{crossed}(t)}{\Delta t}} \quad (4)$$

where the $x(t+\Delta t)$ are calculated under the assumption of no crossing.

A "snapshot" of acceleration and beam sheet velocity is shown in Fig. XIII-21. In this case $t = 300.4\ \omega_p^{-1}$, $\omega_{pb}^2 = \omega_{pp}^2/200$ and $\nu = 0.2\ \omega_p$. This large value of ν was required to keep the plasma linear ($\rho_{1p}/\rho_{0p} = v_{1p}/v_0 = 0.035$ at peak acceleration). From linear theory we would expect an exponential growth rate in space, under the assumption of a steady state, of $\frac{\omega_{pb}}{v_0}\sqrt{\frac{\omega_p}{2\nu}}$, or, for our numbers, a doubling every wavelength. This is seen to be correct for small values of x. Both the acceleration and beam velocity develop a negative DC value in addition to the exponential growth.

The excited traveling wave has a phase velocity less than that of the beam. Initially, the sheets ride through the troughs and crests of this wave. The beam becomes trapped, however, when the beam velocity modulation builds up so that the minimum beam velocity approaches the wave phase velocity. A large charge bunch forms, although it has a considerable velocity spread. The electric field is maximumly decelerating at this point, thereby resulting in maximum energy transfer to the plasma.

The sheets near the velocity minimum form a "sub-bunch" that is rather tight in velocity, and produces sharp dips in the acceleration for distances considerably beyond the overtaking point. The sub-bunch eventually breaks up, but not until the sheet velocity is less than 20 per cent of the injected velocity.

Those sheets that are between the bunches find themselves in an accelerating field, and many seem to be accelerated into the bunch, and maintain the bunch and a wave component near the linear phase velocity for some distance past overtaking.

Eventually the bunches spread out. Unfortunately, the steady state cannot be assumed to exist for distances beyond x = 280, as determined by comparison with snapshots taken at previous times. The point of diminishing returns has been reached as far as computer time goes, since the time to reach the steady state is proportional to the drift times of the slowest electrons, which have become quite long.

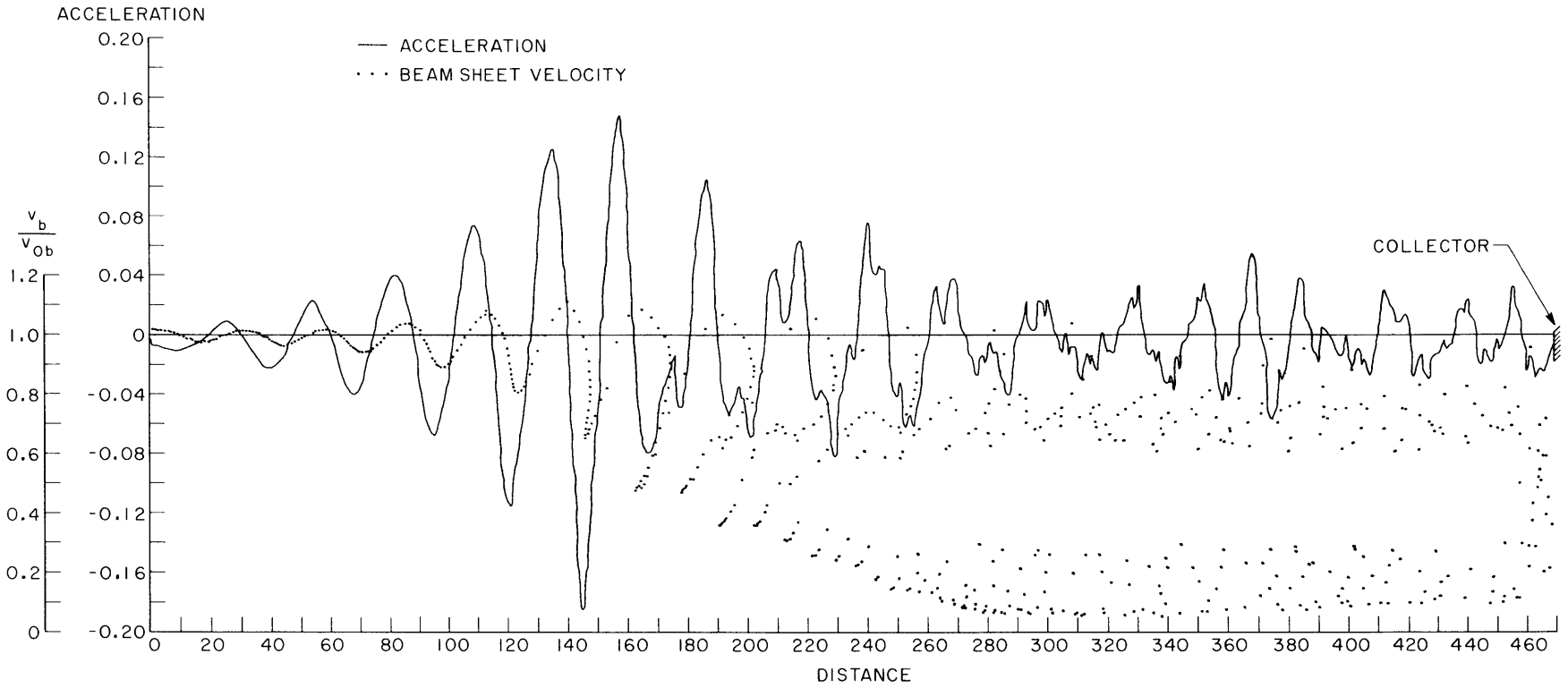

Fig. XIII-21. Acceleration and beam sheet velocity vs distance. Time = 300.4 ω_p^{-1}. Distances are normalized to 0.2 $v_o\omega_p^{-1}$, accelerations to 0.2 $v_o\omega_p$.

Appendix

Derivation of Response of Plasma to a Moving Charge Sheet (Eq. 2)

With the beam considered as free charge and the plasma charge included in the equivalent dielectric constant of Eq. 1, from Poisson's equations, we have

$$E(\omega_1 k) = \frac{\rho(\omega, k)}{-ik\epsilon(\omega, k)}, \tag{A1}$$

where

$$\rho(z, t) = qu_o(z - v_o t). \tag{A2}$$

Performing a Laplace transform in time and a Fourier transform in space, we have

$$\rho(\omega, k) = \frac{q}{i(\omega - kv_o)}, \tag{A3}$$

so that

$$E(\omega, k) = \frac{q}{k\left(\omega - kv_o\right)\left(\omega - \frac{i\nu}{2} + \omega_o\right)\left(\omega - \frac{i\nu}{2} - \omega_o\right)\epsilon_o}. \tag{A4}$$

Here, ω_o is defined by Eq. 3. The pole in the k-plane at ω/v_o is taken for positive z by the Bers-Briggs[2] criterion. This pole introduces a delay in time of z/v_o. The pole at $k = 0$ is not placed by this criterion, but splitting this pole is found to give physically meaningful results. The poles in the ω plane at $\pm\omega_o + i\nu/2$ are easily evaluated by Cauchy's theorem. The result, for $z > 0$, is

$$E(z, t) = -\frac{q}{\epsilon_o} e^{-\frac{\nu}{2}(t - z/v_o)} \cos\left[\omega_o(t - z/v_o) - \tan^{-1}\frac{\nu}{2\omega_o}\right] u_{-1}(t - z/v_o)$$

$$+ \frac{q}{2\epsilon_o} e^{-\frac{\nu}{2}t} \cos\omega_o\left(t - \tan^{-1}\frac{\nu}{2\omega_o}\right) u_{-1}(t), \tag{A5a}$$

and, for $z < 0$,

$$E(z_1 t) = -\frac{q}{2\epsilon_o} 2^{-\frac{\nu}{2}t} \cos\left(\omega_o t - \tan^{-1}\frac{\nu}{2\omega_o}\right) u_{-1}(t). \tag{A5b}$$

The terms independent of z arise from the Laplace transform, in which the sheets are assumed to appear suddenly to t = 0. These terms are ignored, which means that the model assumes that a nonmoving ion sheet appears at z = 0 with the electron sheet.

The z/v_o term in (A5b) can be generalized to an arbitrary $t_1(z)$, where $t_1(z)$ is the time at which the sheet crosses the plane $z\left(\frac{\partial t_1(z)}{\partial z} > 0\right)$. $\rho(z,t)$ must be written

$$\rho(z,t) = q\frac{\partial t_1(z)}{\partial z}\, u_o[t-t_1(z)]. \tag{A6}$$

This is necessary if $\int dz\, \rho(z,t) = q$. Hence

$$\rho(\omega,k) = \int_0^\infty dz\, e^{ikz} \int_0^\infty e^{-i\omega t}\, dt\, q\frac{\partial t_1(z)}{\partial z}\, u_o[t-t_1(z)].$$

Integrating by parts and noting that

$$\frac{d\, \exp[-i\omega t_1(z)]}{dz} = -i\omega \frac{dt_1}{dz}\, e^{-i\omega t_1(z)}, \tag{A7}$$

we obtain

$$\rho(\omega,k) = \frac{q}{i\omega} + \frac{kq}{\omega}\int_0^\infty e^{ikz}\, e^{-i\omega t_1(z)}\, dz. \tag{A8}$$

Inserting this into (A1), we obtain finally

$$E(\omega,k) = -\frac{q}{i\omega\epsilon(\omega,k)} \int_0^\infty dz\, e^{ikz}\, e^{-i\omega t_1(z)} + \frac{q}{\omega k\epsilon(\omega,k)}. \tag{A9}$$

If we take the transform of Eq. 2, we shall find it identical to the first term of (A9). The second term yields the spatially invariant response.

J. A. Davis

References

1. J. A. Davis, Quarterly Progress Report No. 80, Research Laboratory of Electronics, M.I.T., January 15, 1966.
2. R. J. Briggs, Electron-Stream Interaction with Plasmas (The M.I.T. Press, Cambridge, Mass., 1964).

6. THEORY OF PLASMA EXCITATION BY A LINE-CHARGE SOURCE

We are interested in excitation of the beam-plasma discharge (BPD) by a modulated beam.[1,2] In the last report[3] we considered the following theoretical model: Assume a linearized hydrodynamic representation of a fully ionized macroscopically neutral electron-ion plasma, with a longitudinal DC magnetic field, $B_o \vec{i}_z$. The unbounded plasma is excited by a sinusoidally varying line-charge source oriented parallel to the DC magnetic field, $\rho = \rho_o \delta(x)\,\delta(y)$, for $\exp(j\omega t)$ sinusoidal steady-state time dependence. The constant ρ_o is in units of coulombs per meter. We are interested in quasi-static solutions that have azimuthal symmetry and no longitudinal variation.

The set of equations used to describe the system is solved by using Fourier transform theory. The set of equations and the spatial Fourier transforms of the first-order densities, potential, and velocities have been given previously.[3]

This report presents the exact solutions to the problem outlined above. The expressions for the first-order ion velocity and density and the first-order electric field follow.

$$v_{ir}(r) = \left\{ \frac{j\rho_o e\omega\left(-\omega^2+\omega_{ce}^2\right)}{2\pi m_i \epsilon_o\left[\left(-\omega^2+\omega_{pe}^2+\omega_{ce}^2\right)\left(-\omega^2+\omega_{pi}^2+\omega_{ci}^2\right)-\omega_{pe}^2\omega_{pi}^2\right]} \frac{1}{r} \right.$$

$$+ \frac{\rho_o e\omega\left(k_1^2u_e^2-\omega^2+\omega_{ce}^2\right)}{4m_i\epsilon_o\left[u_e^2\left(k_1^2u_i^2-\omega^2+\omega_{ci}^2+\omega_{pi}^2\right)+u_i^2\left(k_1^2u_e^2-\omega^2+\omega_{ce}^2+\omega_{pe}^2\right)\right]} \frac{H_1^{(2)}(k_1r)}{k_1}$$

$$\left. + \frac{\rho_o e\omega\left(k_2^2u_e^2-\omega^2+\omega_{ce}^2\right)}{4m_i\epsilon_o\left[u_e^2\left(k_2^2u_i^2-\omega^2+\omega_{ci}^2+\omega_{pi}^2\right)+u_i^2\left(k_2^2u_e^2-\omega^2+\omega_{ce}^2+\omega_{pe}^2\right)\right]} \frac{H_1^{(2)}(k_2r)}{k_2} \right\} \tag{1}$$

$$v_{i\theta}(r) = \left(j\frac{\omega_{ci}}{\omega}\right) v_{ir}(r) \tag{2}$$

$$n_i(r) = \left\{ \frac{-j\rho_o\omega_{pi}^2\left(k_1^2u_e^2-\omega^2+\omega_{ce}^2\right)}{4e\left[u_e^2\left(k_1^2u_i^2-\omega^2+\omega_{ci}^2+\omega_{pi}^2\right)+u_i^2\left(k_1^2u_e^2-\omega^2+\omega_{ce}^2+\omega_{pe}^2\right)\right]} H_o^{(2)}(k_1r) \right.$$

$$\left. - \frac{j\rho_o\omega_{pi}^2\left(k_2^2u_e^2-\omega^2+\omega_{ce}^2\right)}{4e\left[u_e^2\left(k_2^2u_i^2-\omega^2+\omega_{ci}^2+\omega_{pi}^2\right)+u_i^2\left(k_2^2u_e^2-\omega^2+\omega_{ce}^2+\omega_{pe}^2\right)\right]} H_o^{(2)}(k_2r) \right\} \tag{3}$$

$$E_r(r) = \left\{ \frac{\rho_o\left(-\omega^2+\omega_{ci}^2\right)\left(-\omega^2+\omega_{ce}^2\right)}{2\pi\epsilon_o\left[\left(-\omega^2+\omega_{pe}^2+\omega_{ce}^2\right)\left(-\omega^2+\omega_{pi}^2+\omega_{ci}^2\right)-\omega_{pe}^2\omega_{pi}^2\right]} \frac{1}{r} \right.$$

$$+ \frac{j\rho_o\left(k_1^2u_i^2-\omega^2+\omega_{ci}^2\right)\left(k_1^2u_e^2-\omega^2+\omega_{ce}^2\right)}{4\epsilon_o\left[u_e^2\left(k_1^2u_i^2-\omega^2+\omega_{ci}^2+\omega_{pi}^2\right)+u_i^2\left(k_1^2u_e^2-\omega^2+\omega_{ce}^2+\omega_{pe}^2\right)\right]} \frac{H_1^{(2)}(k_1r)}{k_1}$$

$$\left. + \frac{j\rho_o\left(k_2^2u_i^2-\omega^2+\omega_{ci}^2\right)\left(k_2^2u_e^2-\omega^2+\omega_{ce}^2\right)}{4\epsilon_o\left[u_e^2\left(k_2^2u_i^2-\omega^2+\omega_{ci}^2+\omega_{pi}^2\right)+u_i^2\left(k_2^2u_e^2-\omega^2+\omega_{ce}^2+\omega_{pe}^2\right)\right]} \frac{H_1^{(2)}(k_2r)}{k_2} \right\} \tag{4}$$

where $H^{(2)}$ is the Hankel function of the second kind and of the indicated order and argument.

The expressions for v_{er} and n_e are obtained from Eqs. 1 and 3 by the following manipulations: (a) replace the subscript e with i, (b) replace the subscript i with e, and (c) replace e with -e. The velocity $v_{e\theta}$ is obtained from

$$v_{e\theta} = \left(-j\frac{\omega_{ce}}{\omega}\right) v_{er} \tag{5}$$

The propagation constants k_1 and k_2 are zeros of the dispersion relation $D(k_T) = 0$, that is, values of k_T for which

$$D(k_T) = \left[\left(k_T^2u_i^2-\omega^2+\omega_{ci}^2+\omega_{pi}^2\right)\left(k_T^2u_e^2-\omega^2+\omega_{ce}^2+\omega_{pe}^2\right)-\omega_{pi}^2\omega_{pe}^2\right] \tag{6}$$

is equal to zero. The constants k_1 and k_2 are either positive real or negative imaginary, dependent upon choice of operating frequency ω. The frequencies for which k_1 or k_2 are zero (the cutoff frequencies) satisfy the following equation:

$$\left[\left(-\omega^2+\omega_{ci}^2+\omega_{pi}^2\right)\left(-\omega^2+\omega_{ce}^2+\omega_{pe}^2\right)-\omega_{pi}^2\omega_{pe}^2\right] = 0. \tag{7}$$

We are particularly interested in finding the frequencies at which the ion response to the line-charge excitation is maximum. Note that the constants k_1 and k_2 appear in the arguments of the Hankel functions, so that at cutoff frequencies the responses are infinite. For very low densities or very high magnetic field the lower of the two cutoff frequencies is near the ion cyclotron frequency. For very high densities it becomes the lower hybrid frequency. For plasmas encountered in the BPD systems, however, this cutoff frequency is at least an order of magnitude greater than the ion cyclotron frequency, in the range 10-100 Mc. The second cutoff frequency is somewhat above the

electron plasma frequency, for typical BPD parameters.

Note that the terms with Hankel functions contain bracketed factors involving the thermal velocities u_i and u_e. By proper choice of operating frequency, this term can cause the responses of the system to approach infinity. If the operating frequency is above cutoff, this frequency is greater than the ion plasma frequency. Below cutoff this value of ω^2 is less than ω_{pi}^2.

It appears from this analysis that large response to the line charge excitation can be obtained by choosing the operating frequency close to a cutoff frequency. This theoretical model may fail, however, near a cutoff frequency, where the first-order magnetic field becomes important. For this reason, we are in the process of including first-order magnetic field in our model. Numerical evaluation of the results given here is also in progress.

G. D. Bernard

References

1. L. D. Smullin, "Beam-Plasma Discharge: Excitation of Ions at the Ion Cyclotron Frequency (Theory)," Quarterly Progress Report No. 80, Research Laboratory of Electronics, M.I.T., January 15, 1966, pp. 111-113.
2. W. D. Getty and G. D. Bernard, "Beam-Plasma Discharge: Excitation of the Ions at the Ion Cyclotron Frequency (Experiment)," Quarterly Progress Report No. 80, Research Laboratory of Electronics, M.I.T., January 15, 1966, pp. 113-115.
3. G. D. Bernard and A. Bers, "Theory of Plasma Excitation by a Line-Charge Source," Quarterly Progress Report No. 81, Research Laboratory of Electronics, M.I.T., April 15, 1966, pp. 102-104.

7. CROSS-FIELD BEAM-PLASMA INTERACTIONS

This is the first report on a new experiment that has been started in this group. The general object of the experiment is to study the properties of an electron beam with transverse energy comparable to its longitudinal energy. Properties of this beam will be investigated in the presence of varying plasma densities. At present, the basic experimental apparatus has been completed and the electron gun, which will be described in this report, is operating. Some initial observations of the beam current have been made and will be briefly discussed.

Experimental Apparatus

The experiment is being carried on in the pumped vacuum system shown in Fig. XIII-22. The discharge takes place in a Pyrex cross of 4 inches diameter, to the right of the magnetic circuit. The gun and the collector are in the horizontal arms of the cross. Gas can be admitted through the top, and the system is pumped by means

of an oil diffusion pump and a forepump.

As mentioned, the gun is in one of the horizontal arms of the cross. It creates a hollow cylindrical beam of essentially monoenergetic electrons primarily with only axial velocity. This is accomplished by means of a hollow-cathode disk and a Pierce-type grid and anode as shown in Fig. XIII-23. The long and short dashed lines represent an

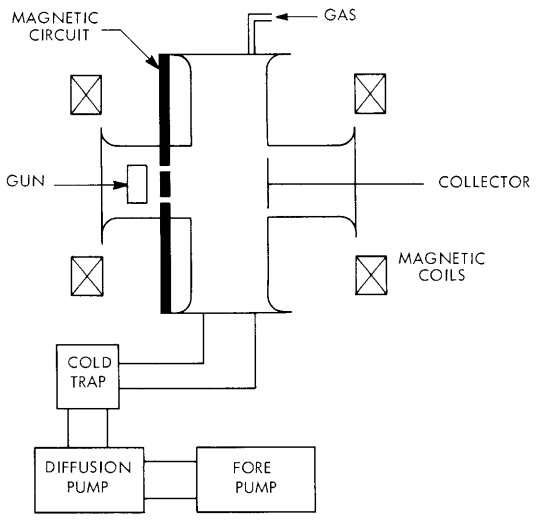

Fig. XIII-22. The System.

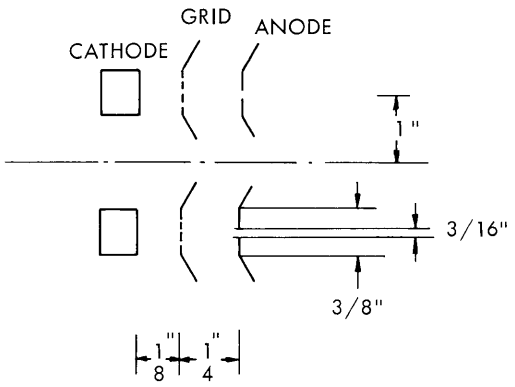

Fig. XIII-23. The Gun.

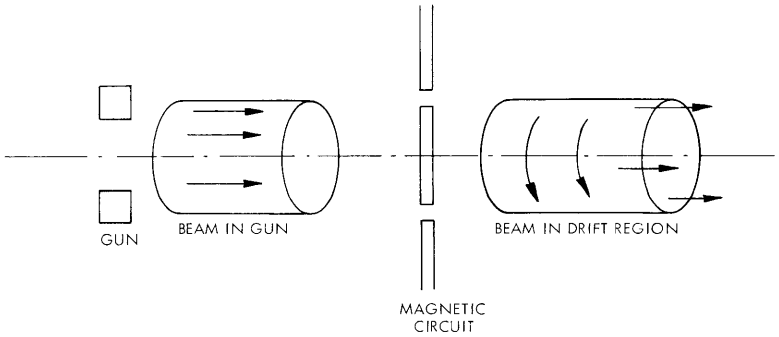

Fig. XIII-24. The Beam.

axis of revolution for the structures shown. The grid is used to control the perveance of the beam.

The beam, which is not intercepted by the anode but passes through it, is injected into a magnetic circuit that alters its velocity distribution. The initial experiments will be carried out by using a hollow cylindrical beam with drift along and rotation about its axis (see Fig. XIII-24). The ratio of transverse energy to axial energy of the beam

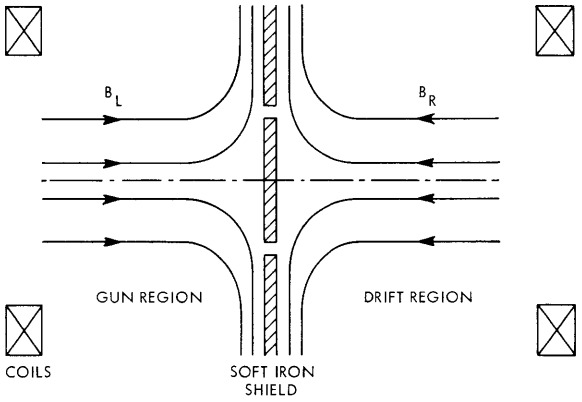

Fig. XIII-25. The magnetic circuit.

can be controlled by adjusting the field in the magnetic circuit.

Magnetic Circuit

The magnetic circuit is composed of a large soft-iron shield which allows the magnetic field in the gun region to be independent of the field in the drift region (see Fig. XIII-25). Ideally, the magnetic flux lines should be along the axis of symmetry except in the magnetic circuit where they should be radial. The beam is injected from the gun region into the drift region through a disk-shaped hole in the soft iron shield. For various relative magnitudes of the magnetic field on the right, B_R, and on the left, B_L, many different

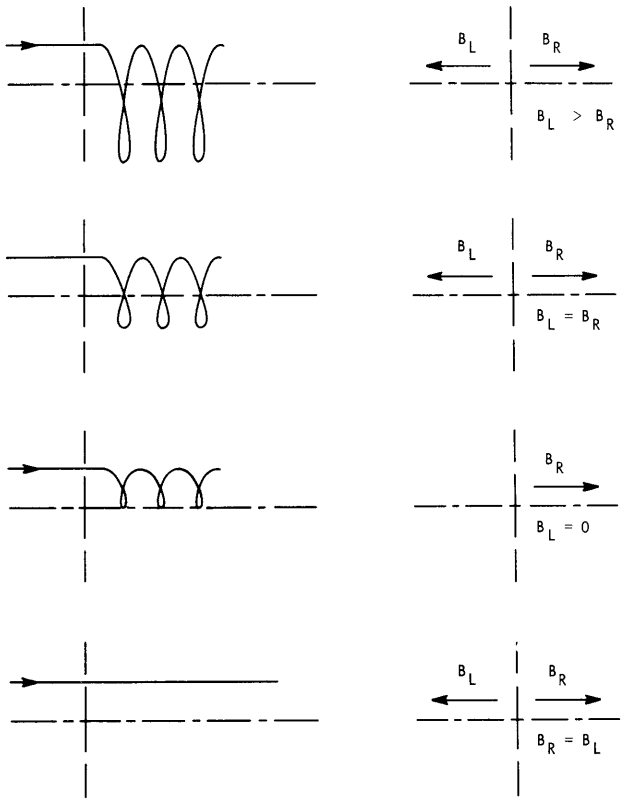

Fig. XIII-26. Beam configurations.

beam configurations can be obtained. In Fig. XIII-26 the trajectory of a single electron injected into the magnetic-field environment described at the right is traced out. The injected electron for all cases has the same total kinetic energy. This kinetic energy

must be greater than a minimum value given by

$$\text{Kinetic energy}_{\min} = \frac{q^2(B_L - B_R)^2 r_o^2}{8\,m},$$

where q is the charge, m the mass, and r_o the radius of the disk-shaped hole in the soft iron shield. The kinetic energy in excess of this amount goes into longitudinal energy. Therefore to obtain the beam described by Fig. XIII-24, it is necessary to make B_L and B_R equal in magnitude but oppositely directed.

Initial Measurements

Some of the initial measurements of the beam current have shown an interesting low-frequency oscillation. With a beam voltage of 500 volts and grid voltage of 50-75 volts the emission current varies from 100 ma to 200 ma. Of this emission current, 20-40 ma passed through the anode into the drift region. The magnetic field was adjusted as shown in Fig. XIII-24 to give a rotating hollow beam of approximately 1-inch radius and 1/8 inch thick. The magnetic field in the drift region was 25 gauss. Under these conditions, very clean, 1-2 per cent modulation of the DC collector current was observed in the neighborhood of 100 kc. This modulation was observed for varying degrees of argon plasma density associated with pressures ranging from 10^{-7} to 10^{-5} mm Hg.

B. Kusse, A. Bers

8. DYNAMICS OF THE PLASMA BOUNDARY

Previously, we have given computed trajectories of charge sheets in order to study the nonlinear oscillations of a finite plasma slab in the absence of a magnetic field.[1,2] It was observed that a "scrambling," initiated by a crossing or overtaking of trajectories near the surface, gradually destroyed the coherent oscillations of the entire slab. Leavens and Leavens[3] have derived an expression for the time of the first crossing, t_s, given by $\omega_p t_s = \pi + \sqrt{2}$.

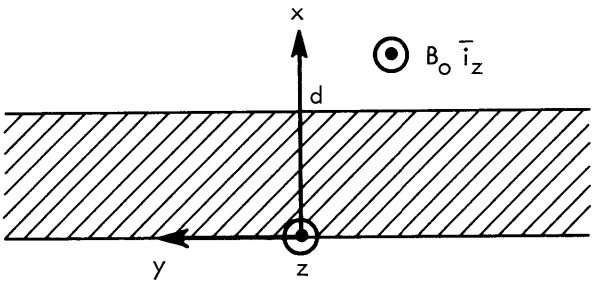

Fig. XIII-27. Plasma slab in equilibrium.

In this report we present a derivation for the time of the first overtaking if the plasma slab is immersed in a DC magnetic field. The results are valid for electron-cyclotron frequencies, ω_c, in the range $0 \leq \omega_c \leq \omega_p$. A graphical technique is used to display the formation of the overtaking for various values of (ω_c/ω_p).

The plasma slab in equilibrium consists of a uniform number density of ions and

electrons distributed over a thickness, d, in the x-direction, but infinite in the y- and z-directions. The important addition is the presence of a DC magnetic field, $B = B_o i_z$, as shown in Fig. XIII-27. The ions are assumed to be infinitely heavy and hence are treated as a rigid slab. The instantaneous position, x, of an electron is a function of its equilibrium position, x_o, and the time, or $x = x(x_o, t)$. We assume that at $t = 0$ all of the electrons have been displaced an amount δ in the x-direction, $x(x_o, 0) = x_o + \delta$, and seek the motion of the electrons for $t > 0$. For simplicity, we study the electrons that were at $y = 0$ at $t = 0$, so $y = y(x_o, t)$.

The equations of motion for the electrons are

$$\frac{d^2x}{dt^2} = -\omega_p^2(x-x_o) - \omega_c \frac{dy}{dt}$$

$$\frac{d^2y}{dt^2} = \omega_c \frac{dx}{dt} \qquad 0 < x < d \qquad (1)$$

$$\frac{d^2x}{dt^2} = \omega_p^2(x_o-d) - \omega_c \frac{dy}{dt}$$

$$\frac{d^2y}{dt^2} = \omega_c \frac{dx}{dt} \qquad x > d \qquad (2)$$

as long as no overtaking has taken place. Here, $\omega_p^2 = \frac{e^2 n_o}{\epsilon_o m}$ and $\omega_c = \frac{eB_o}{m}$, where e is the electronic charge, n_o is the equilibrium particle number density, and m is the mass of an electron.

The solution of Eqs. 1 and 2 is

$$x = x_o + \frac{\omega_c^2 \delta}{\omega_o^2} + \frac{\omega_p^2 \delta}{\omega_o^2} \cos \omega_o t \qquad 0 < x < d, \quad x_o < (d-\delta)$$

$$y = -\frac{\omega_p^2 \omega_c \delta}{\omega_o^3}(\omega_o t - \sin \omega_o t)$$

$$x = x_o + \delta + \frac{\omega_p^2}{\omega_c^2}(x_o-d)(1 - \cos \omega_c t) \qquad x > d, \quad x_o > (d-\delta)$$

$$y = \frac{\omega_p^2}{\omega_c^2}(x_o-d)(\omega_c t - \sin \omega_c t),$$

where $\omega_o^2 = \omega_c^2 + \omega_p^2$.

Electrons that were outside the ion boundary at x = d will go back into the ion background at time t_o, given by

$$\omega_c t_o = \cos^{-1}\left[1 + \frac{\omega_c^2}{\omega_p^2}\left(1 + \frac{\delta}{x_o - d}\right)\right]. \tag{3}$$

After this time these particles have the motion inside described by

$$x = x_o + \frac{\omega_c^2}{\omega_o^2}\delta - \left(x_o - d + \frac{\omega_c^2\delta}{\omega_o^2}\right)\cos\omega_o(t-t_o) + \frac{\omega_p^2(x_o-d)}{\omega_c\omega_o}\sin\omega_c t_o \sin\omega_o(t-t_o) \qquad \begin{matrix} x < 0 \\ x_o > d - \delta \end{matrix}$$

$$y = \frac{-\omega_p^2\omega_c\delta t}{\omega_o^2} - \frac{\omega_c}{\omega_o}\left(x_o - d + \frac{\omega_c^2\delta}{\omega_o^2}\right)\sin\omega_o(t-t_o) + \frac{\omega_p^2 t_o}{\omega_c}\left(x_o - d + \frac{\omega_c^2\delta}{\omega_o^2}\right)$$

$$- \frac{\omega_p^2(x_o-d)}{\omega_o^2}\sin\omega_c t_o \cos\omega_o(t-t_o) - \frac{\omega_p^4(x_o-d)}{\omega_o^2\omega_c^2}\sin\omega_c t_o. \tag{4}$$

The condition for overtaking is $\partial x/\partial x_o = 0$. If t_s denotes the time at which overtaking occurs, the condition for earliest overtaking is $\partial t_s/\partial x_o = 0$.[3]

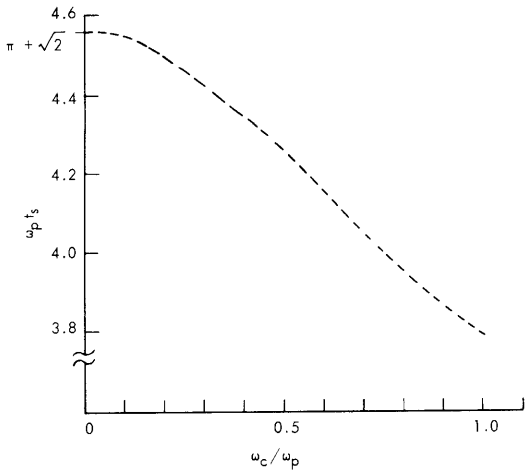

Fig. XIII-28. Overtaking time versus (ω_c/ω_p).

Application of these two conditions to the equations describing the motion of the electrons that have returned to the ion background gives

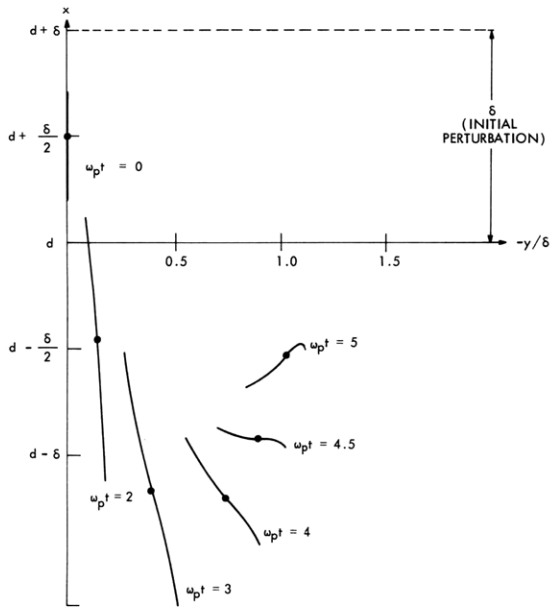

Fig. XIII-29. Onset of overtaking for $\frac{\omega_c}{\omega_p} = 0.2$.

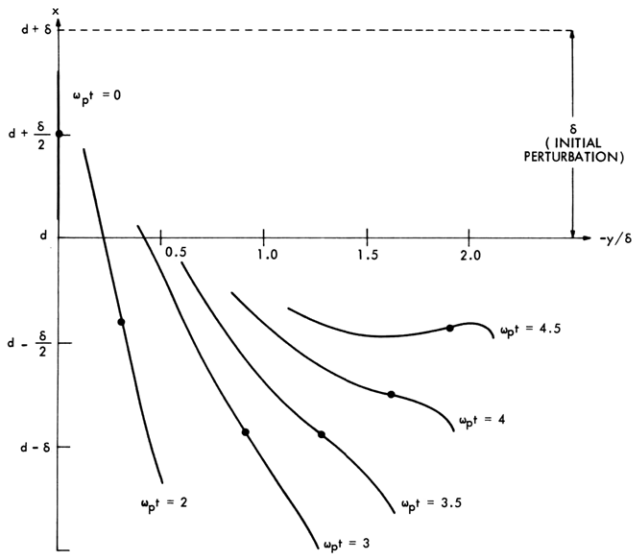

Fig. XIII-30. Onset of overtaking for $\frac{\omega_c}{\omega_p} = 0.5$.

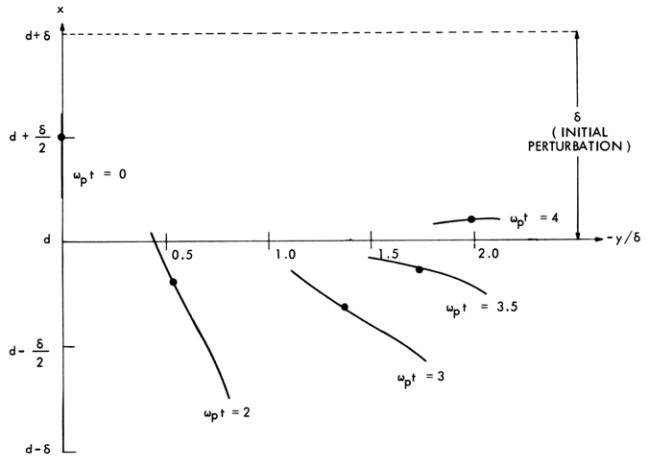

Fig. XIII-31. Onset of overtaking for $\frac{\omega_c}{\omega_p} = 1.0$.

$$-\left(1+\frac{\delta}{x_o-d}\right)\cos\omega_o(t_s-t_o)+\frac{\omega_p^2}{\omega_c\omega_o}\sin\omega_c t_o\sin\omega_o(t_s-t_o)=-1 \tag{5}$$

and

$$\frac{-\omega_p^2\delta}{\omega_o^2(x_o-d)}\omega_o\frac{\partial t_o}{\partial x_o}\sin\omega_o(t_s-t_o)=0. \tag{6}$$

Equations 5 and 6 yield for the overtaking time, t_s,

$$\omega_o t_s=\pi+\frac{\omega_o}{\omega_c}\cos^{-1}\left(1-\frac{\omega_c^2}{\omega_p^2}\right). \tag{7}$$

In Fig. XIII-28 we plot $\omega_p t_s$ as a function of the ratio (ω_c/ω_p). Note that as ω_c/ω_p approaches zero, $\omega_p t_s$ approaches the value $(\pi+\sqrt{2})$, as reported by Leavens and Leavens.[3]

Equations 4 predict that the electron that is first involved in overtaking has the equilibrium position $x_o = d - (1/2)\delta$. The overtaking actually occurs at a position in the ion background given by

$$x=d-\delta\left(\frac{\omega_p^2-\omega_c^2}{\omega_p^2+\omega_c^2}\right). \tag{8}$$

Equation 8 reduces to $x = d - \delta$ as $\omega_c/\omega_p \to 0$, which again agrees with Leavens and Leavens.[3] As ω_c/ω_p increases from zero, the overtaking occurs nearer the surface, until $\omega_c = \omega_p$, when it occurs exactly at $x = d$. The study of the motion has not been carried out for $\omega_c > \omega_p$.

The overtaking can be visualized more easily if we plot electron trajectories as a function of time. If at $t = 0$ a "line" is fixed to the electrons along $y = 0$ and to those that are in the vicinity of $x = d + \frac{1}{2}\delta$, the onset of overtaking can be seen if the deformation of this "line" is followed as a function of time. Figures XIII-29, XIII-30, and XIII-31 illustrate this approach for $\omega_c/\omega_p = 0.2$, $\omega_c/\omega_p = 0.5$, and $\omega_c/\omega_p = 1$, respectively.

It is important to note that we have only studied the overtaking that occurs near the surface of the ion background at $x = d$. An extension of the techniques used here must be made to determine when overtaking occurs for particles near the other boundary, namely $x = 0$.

H. M. Schneider

References

1. H. M. Schneider, "Dynamics of the Plasma Boundary," Quarterly Progress Report No. 80, Research Laboratory of Electronics, M.I.T., January 15, 1966, pp. 128-129.

2. H. M. Schneider and A. Bers, "Dynamics of the Plasma Boundary," Quarterly Progress Report No. 78, Research Laboratory of Electronics, M.I.T., July 15, 1965, pp. 114-119.

3. W. M. Leavens and I. B. Leavens, Bull. Am. Phys. Soc. 1, 480 (1962).

XIII. PLASMAS AND CONTROLLED NUCLEAR FUSION*

B. Applied Plasma Physics Related to Controlled Nuclear Fusion

Academic and Research Staff

Prof. D. J. Rose
Prof. T. H. Dupree
Prof. L. M. Lidsky
Prof. E. P. Gyftopoulos

Graduate Students

R. W. Flynn
R. A. Hill
C. S. Ribbeck
C. E. Wagner
J. C. Woo

1. GENERATION OF A QUIESCENT ARC PLASMA

In our experimental study of the highly ionized plasma produced by a hollow cathode discharge, we have been able to produce a steady-state variable parameter, highly ionized plasma of density $10^{12} \leq n \leq 10^{14}$/c.c. and $T_i < T_e \leq 20$ ev that operates quiescently in a strong magnetic field of several kilogauss. Because of the apparent low noise and the adjustability of the operating parameters, this device possesses some advantages over the Q-machine commonly used for studies of highly ionized plasmas.

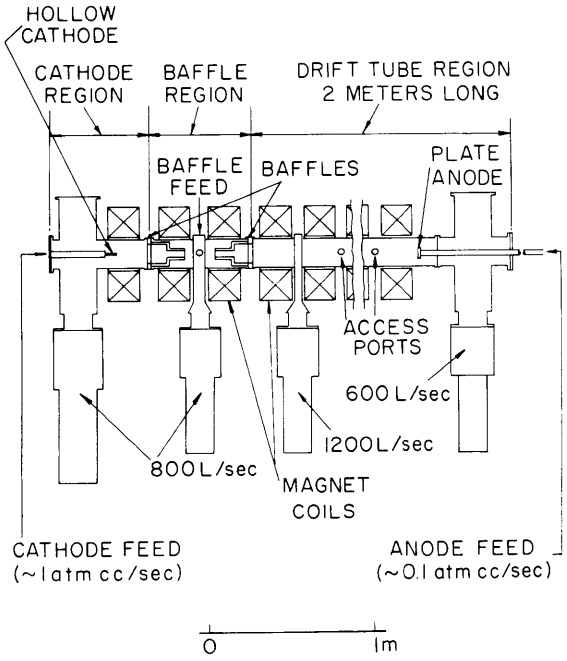

Fig. XIII-32. Schematic view of the apparatus.

The apparatus, described in detail in a previous report,[1] is shown schematically in Fig. XIII-32 and consists of an arc column driven by a hollow cathode discharge at the left. Plasmas of this type often exhibit large scale fluctuations due to instabilities arising from differential drifts. Because the operation of the discharge requires high neutral density and strong electric field near the cathode, oscillations are generally excited at this source region and suppressions of the instability at the original locale is not feasible. The low noise and the high degree of ionization features of the plasma result from the considerable separation of the drift-tube working region from the plasma-generation region by a double baffle chamber that damps

*This work was supported by the National Science Foundation (Grant GK-614).

fluctuations originating at the cathode.

Analysis on such a plasma column in a strong magnetic field has shown that in the weakly ionized state the plasma is unstable against the well-known convective modes (see Kadomstev and Nedospasov). As the value of the ion confinement factor (the dimensionless product of the ion-cyclotron frequency and the ion-collision time) increases, a universal mode dominates and only perturbations of longer and longer wavelength can be unstable.[2] Therefore, in a plasma column of finite dimensions, the system can be operated stably without excitation drift waves.

In order to achieve this condition, it is only necessary to apply a sufficiently strong magnetic field in the baffle region, and at the same time to maintain the neutral pressure low in the working region. The effect of the magnetic field in the baffle region on the frequency spectrum of the fluctuations is clearly demonstrated by the isometric plot of the noise spectrum versus magnetic field, as picked up by a floating electrostatic probe shown in Fig. XIII-33. A strong magnetic field is increased, the dominant harmonics are severely damped and only low-level white noise remains. The effect on the plasma in the working region is illustrated in Figs. XIII-34 and XIII-35 which show the fluctuations in the probe current at various bias. When instabilities are excited in the baffle region, the fluctuations propagate into the drift tube as shown in Fig. XIII-34. When the conditions in the baffle are such that fluctuations are damped there, however, the fluctuation level of the plasma in the drift tube is remarkably low ($\sim 1\%$ rms) and exhibits no dominant frequency. Furthermore, the plasma in the drift tube, which is highly ionized, remains quiescent, irrespective of the magnetic field strength applied there if the neutral background is kept low by rapid pumping.

Since the fluctuation level depends on the magnetic field strength in the baffle region and the background pressure in the drift tube, we show in Fig. XIII-36 a contour map of constant rms noise level in such a space. The map demonstrated our previous remarks regarding the ingredients for the quiescent operation of such a plasma. In order to obtain a high plasma density in the drift tube, a supplementary anode feed was used. Therefore, in Fig. XIII-36 where the contour lines are closely spaced near 10^{-4} torr, the sharp rise in the percentage of fluctuations was not due to increase of fluctuation level (it remains relatively constant), but rather to drop in the steady-state density as the anode feed is cut off. A significant extension of the quiescent operating regime can be achieved by the addition of baffles to isolate the end-plate anode from the working region.

The successful generation of such a plasma represents an experimental demonstration of theoretical predictions of instabilities attributable to differential Hall

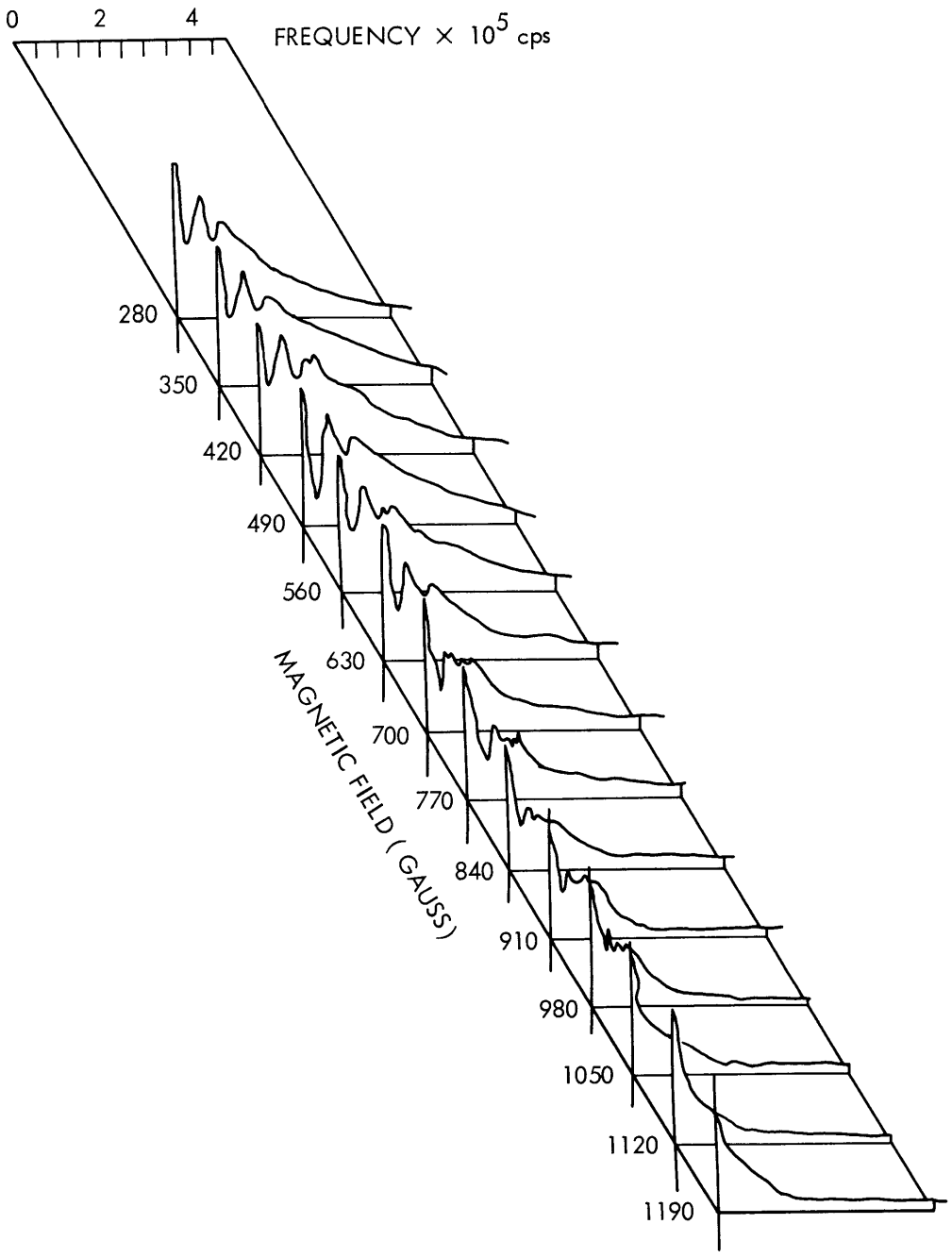

Fig. XIII-33. Noise spectrum vs magnetic field.

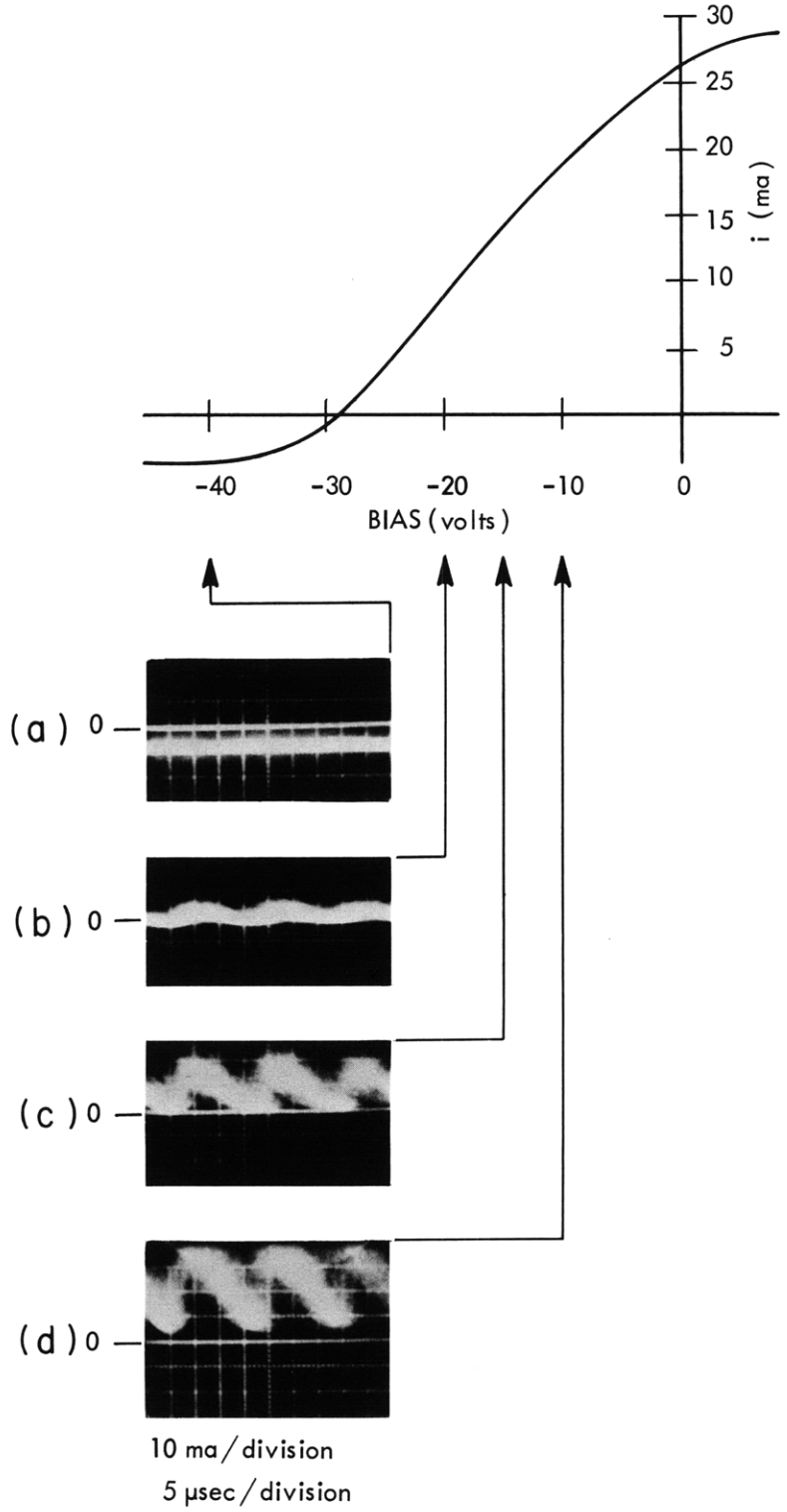

Fig. XIII-34. Probe current in the drift tube with instabilities excited.

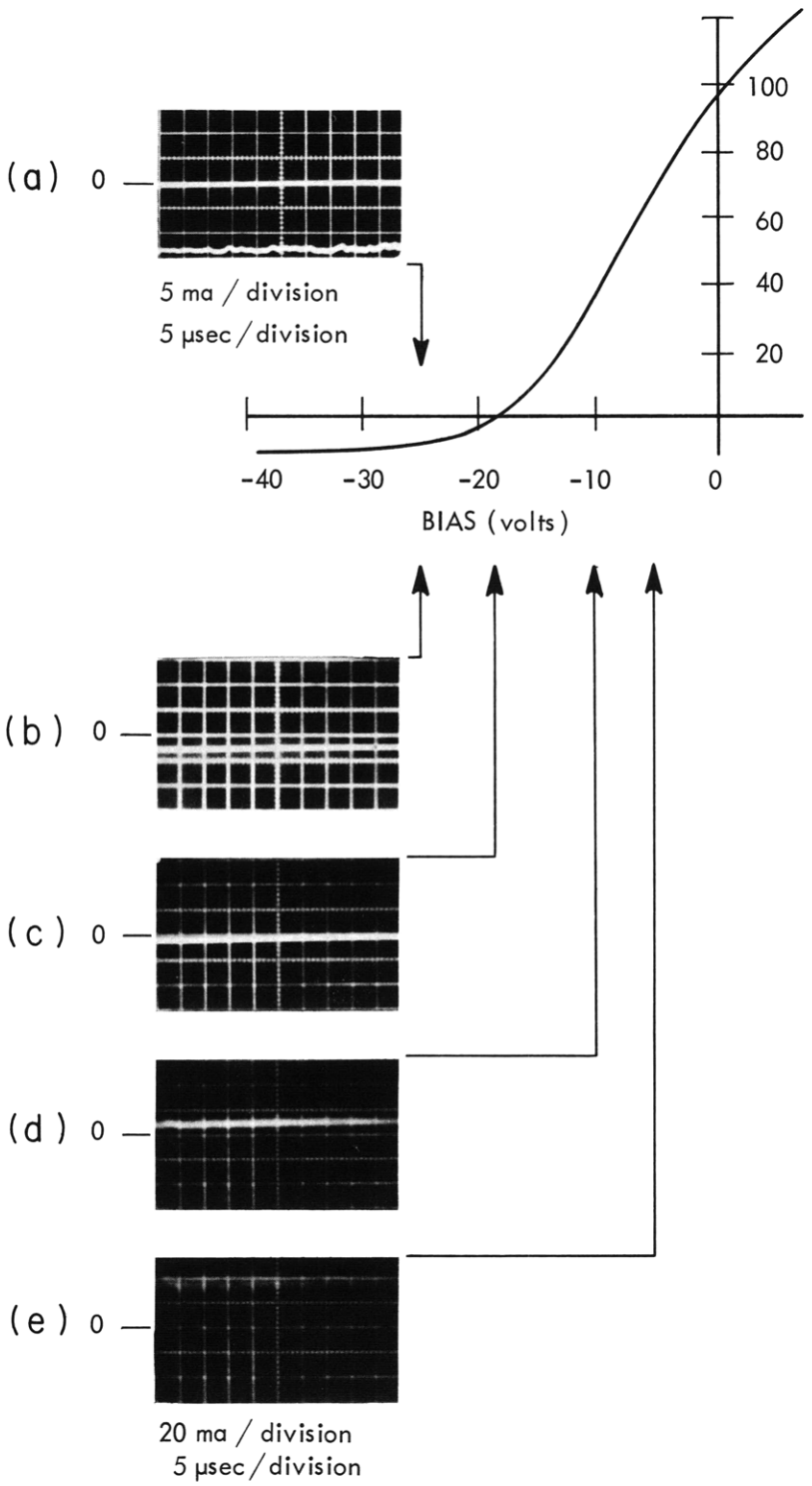

Fig. XIII-35. Probe current in the drift tube during quiescent operation.

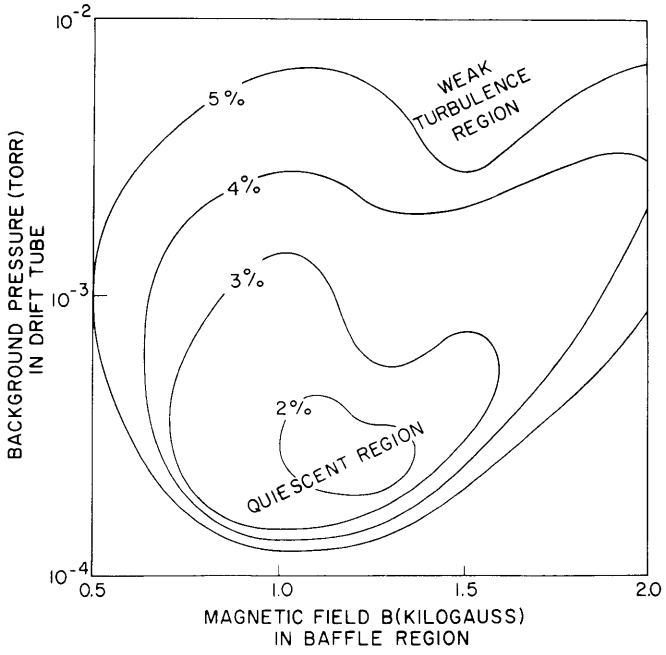

Fig. XIII-36. Contour map of constant rms noise level.

Table XIII-3. Comparison of parameters.

Operating Parameters	Hollow Cathode	Q-Machine	Stellarator
Plasma density n_o (m^{-3})	$<10^{14}$	$<10^{11}$	10^{12}
Electron temperature T_e(ev)	10	0.2	50
Ion temperature T_i (ev)	~1	0.2	0.2 - 100
Magnetic field B (gauss)	10^3	10^3	$1 - 4 \times 10^4$
Plasma dimensions			
R (m)	0.1	0.1	0.1
L (m)	1.0	1.0	10
Scaling Parameters			
$n_o \lambda d^3$ (in a Debye sphere)	10^3	10^2	10^5
$(\omega_{pe}/\omega_{ce})^2$	10^2	1	10^{-2}
$\omega_c \tau_e$	10^3	10^{-2}	10^6
$\omega_{ci} \tau_i$	10	10^{-6}	10

drift. Of greater interest, however, is the quiescent plasma itself whose parameters make it a versatile apparatus for experimental studies of plasma physics. In Table XII-3 we summarize the operating and scaling parameters of several plasma systems for comparison.

J. C. Woo, D. J. Rose

References

1. J. C. Woo, Quarterly Progress Report No. 81, Research Laboratory of Electronics, M.I.T., April 15, 1966, pp. 115-121.
2. J. C. Woo (unpublished data).

2. UNIVERSAL INSTABILITY IN A COLLISION-DOMINATED PLASMA

In our analysis of the stability of a highly ionized plasma column, we have rediscovered,[1] and now interpreted, a destabilizing effect arising purely from the existence of a density gradient which in turn produces charge-separation fields that drive plasma into the initial density perturbation. We present here a simple physical derivation for the stability criteria that clearly illustrates the mechanism of this instability.

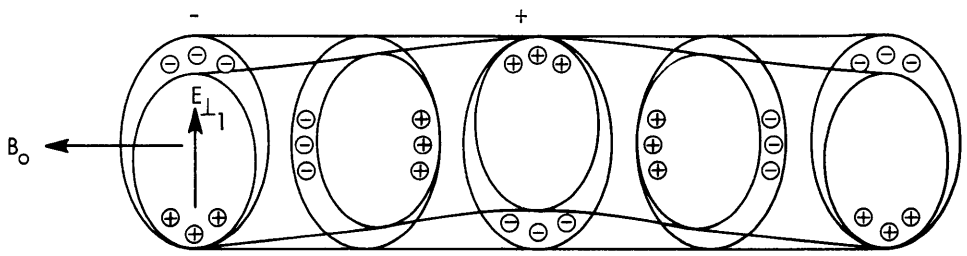

Fig. XIII-37. Effect of perturbing the long plasma column.

Consider a long plasma column confined by a steady magnetic field B_o in a vacuum tube of transverse dimension x_o. The length of the tube is infinite and the plasma is inhomogeneous only in the radial direction with the density given by

$$n_o = N_o \exp(-x/p). \tag{1}$$

Let this column be perturbed slightly as shown in Fig. XIII-37, then there is a density fluctuation n_1 along the field lines and the plasma electrons diffuse from the high-density region to the low-density region. The massive ions remain in the original locale; thus a potential

$$\phi_1 = T_e n_1 / n_o \tag{2}$$

is set up between the maximum and minimum density points along the field line. This potential difference also appears across the plasma column as a transverse electric field,

$$E_{\perp_1} = T_e n_1 / n_o p, \tag{3}$$

in the direction shown.

This first-order electric field $E_{\perp_1}$ produces a drift of the entire plasma column in the $E_{\perp_1} \times B_o$ direction as shown in Fig. XIII-38. Because of the difference in the Hall mobility of the electrons $b_e/\omega_e \tau_e$ and of the ions $\omega_i \tau_i b_i / \left(1+\omega_i^2 \tau_i^2\right)$, a charge imbalance grows at the rate

$$\frac{\partial}{\partial t}[e(n_e - n_i)] = \left[\frac{b_e}{\omega_e \tau_e} - \frac{\omega_i \tau_i b_i}{\left(1+\omega_i^2 \tau_i^2\right)}\right] \frac{T_e}{p_z} n_i . \tag{4}$$

Here, ω_e and ω_i are the cyclotron frequencies, and τ_e and τ_i are the collision times of the electrons and ions.

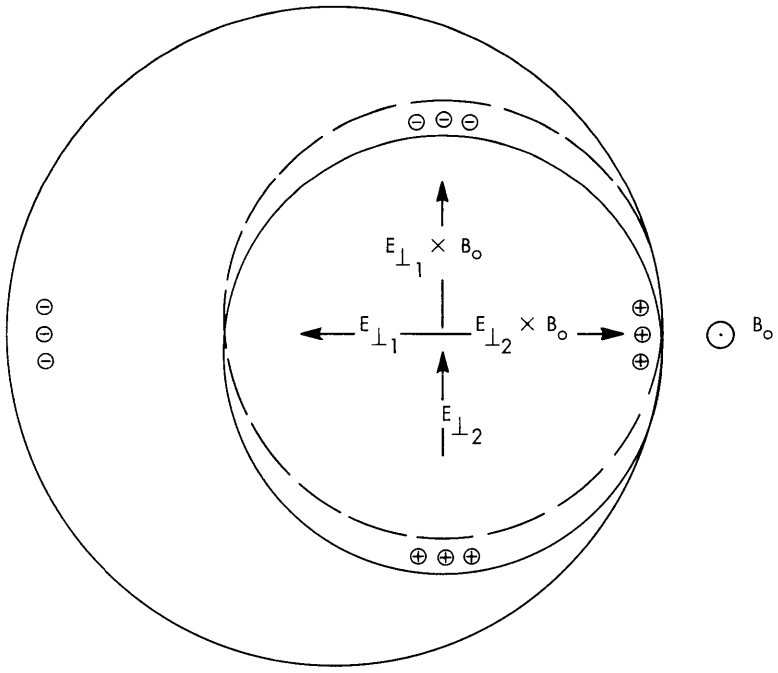

Fig. XIII-38. Drift of plasma column produced by first-order electric field $E_{\perp_1}$.

The electric field $E_{\perp_2}$ resulting from the charge separation accelerates the plasma ions into the initial perturbation n_1 at the rate

$$\frac{\partial^2}{\partial t^2} n_1 = \frac{\omega_i \tau_i b_i}{\left(1+\omega_i^2 \tau_i^2\right)} \frac{\partial E_{\perp_2}}{\partial t} \nabla \cdot n_o$$

$$= \frac{\omega_i \tau_i b_i}{\left(1+\omega_i^2 \tau_i^2\right)} \frac{e}{\epsilon_o} T_e \frac{n_o}{p} \frac{n_1}{p^2} \left[\frac{b_e}{\omega_e \tau_e} - \frac{\omega_i \tau_i b_i}{\left(1+\omega_i^2 \tau_i^2\right)} \right] \tag{5}$$

which accounts for the growth of the perturbation.

The stability criteria are determined by the competition between this growth rate and the damping effects. The charge imbalance produces a second potential also of the order of $T_e n_1/n_o$. The ion transverse current from that resulting electric field, plus electron axial current, tends to reduce the charge build-ups. The net stabilizing flow is

$$\left[b_e k^2 + \frac{b_i}{\left(1+\omega_i^2 \tau_i^2\right)} \gamma^2 \right] T_e n_o .$$

Thus the growth rate of the electric field $E_{\perp_2}$ is reduced, and the damping effect on the density perturbation is given by

$$-\frac{\partial^2 n_1}{\partial t^2} = b_i \frac{e}{\epsilon_o} T_e n_1 \left[k^2 b_e + \frac{b_i}{\left(1+\omega_i^2 \tau_i^2\right)} \gamma^2 \right] \frac{n_o}{p} . \tag{6}$$

The net rate of change of the density perturbation is, therefore,

$$\frac{\partial^2 n_1}{\partial t^2} = \left\{ \frac{\omega_i \tau_i}{\left(1+\omega_i^2 \tau_i^2\right)} \left[\frac{b_e}{\omega_e \tau_e} - \frac{\omega_i \tau_i b_i}{\left(1+\omega_i^2 \tau_i^2\right)} \right] \frac{1}{p^2} - \left[b_e k^2 + \frac{b_i}{\left(1+\omega_i^2 \tau_i^2\right)} \gamma^2 \right] \right\} \frac{e}{\epsilon_o} T_e n_1 \frac{n_o}{p} b_i \tag{7}$$

from which we obtain the stability criterion

$$\frac{p^2 \left[b_e k^2 + \frac{b_i}{\left(1+\omega_i^2 \tau_i^2\right)} \gamma^2 \right] \left(1+\omega_i^2 \tau_i^2\right)}{\omega_i \tau_i \left[\frac{b_e}{\omega_e \tau_e} - \frac{\omega_i \tau_i b_i}{\left(1+\omega_i^2 \tau_i^2\right)} \right]} > 1. \tag{8}$$

A more rigorous analysis[2] gives for the stability criterion

$$p^2 \frac{k^2}{\gamma^2} \frac{\left[T_e\left(\frac{\pi^2}{x_o^2}+\gamma^2+\frac{1}{2p^2}\right)+T_i\left(\frac{\pi^2}{x_o^2}+\gamma^2\right)\right]\left[b_e k^2+\frac{b_i}{\left(1+\omega_i^2\tau_i^2\right)}\left(\frac{\pi^2}{x_o^2}+\gamma^2+\frac{1}{2p^2}\right)\right]}{\left[\omega_i\tau_i k^2 T_e - T_i\left(\frac{\tau^2}{x_o^2}+\gamma^2\right)\frac{1}{\left(1+\omega_i^2\tau_i^2\right)}\right]\left[\frac{b_e}{\omega_e\tau_e}-\frac{\omega_i\tau_i b_i}{\left(1+\omega_i^2\tau_i^2\right)}\right]}. \quad (9)$$

In the limit $T_i = 0$ and with differences in the geometric factors in p, $1/\gamma$ and x_o ignored, Eqs. 8 and 9 are identical except for a factor $\left(1+\omega_i^2\tau_i^2\right)$, which is of the order of unity in the regime where this instability is important.

Since the growth of the perturbation requires the feeding of the ions into the original perturbation via Hall mobility and the perturbed field $E_{\perp_2}$, this instability can occur only when $\omega_i^2\tau_i^2 \sim 1$. If $\omega_i^2\tau_i^2 \gg 1$, the differential drift vanishes and no charge seperation can occur. We note that the instability is initiated by the development of a longitudinal electric field because of the rapid diffusion of the electrons, and therefore the instability is analogous to the destabilization caused by longitudinal electron thermal conductivity (called "thermal Force" in Russian publications) considered by Galeev, Oraveskii, and Sagdeev.[1]

J. C. Woo, D. J. Rose

References

1. A. A. Galeev, V. N. Oraveskii and R. Z. Sagdeev Soviet Phys. – JETP 17, 615 (1963).
2. J. C. Woo (unpublished).